Range shortening, radiation transport, and Rayleigh-Taylor instability phenomena in ion-beam-driven inertial-fusion-reactor-size targets: Implosion, ignition, and burn phases

Keith A. Long
Institute de Génie Atomique, Département de Physique, Ecole Polytechnique Fédérale de Lausanne, PHB-Ecublens, CH-1015 Lausanne, Switzerland

Naeem A. Tahir
International Centre for Theoretical Physics, 11 strada Costiera, Miramare, P.O. Box 586, I-34100 Trieste, Italy
(Received 8 August 1985; revised manuscript received 6 October 1986)

In this paper we present an analysis of the theory of the energy deposition of ions in cold materials and hot dense plasmas together with numerical calculations for heavy and light ions of interest to ion-beam fusion. We have used the GORGON computer code of Long, Moritz, and Tahir (which is an extension of the code originally written for protons by Nardi, Peleg, and Zinamon) to carry out these calculations. The energy-deposition data calculated in this manner has been used in the design of heavy-ion-beam-driven fusion targets suitable for a reactor, by its inclusion in the MEDUSA code of Christiansen, Ashby, and Roberts as extended by Tahir and Long. A number of other improvements have been made in this code and these are also discussed. Various aspects of the theoretical analysis of such targets are discussed including the calculation of the hydrodynamic stability, the hydrodynamic efficiency, and the gain. Various different target designs have been used, some of them new. In general these targets are driven by Bi^+ ions of energy 8—12 GeV, with an input energy of 4—6.5 MJ, with output energies in the range 600—900 MJ, and with gains in the range 120—180. The peak powers are in the range of 500—750 TW. We present detailed calculations of the ablation, compression, ignition, and burn phases. By the application of a new stability analysis which includes ablation and density-gradient effects we show that these targets appear to implode in a stable manner. Thus the targets designed offer working examples suited for use in a future inertial-confinement fusion reactor.

I. INTRODUCTION

There has been a growing interest in the employment of ions for use as a driver for inertial-confinement fusion[1—47] and as a means of producing hot dense plasmas for basic research.[20—24] The use of ions for inertial-confinement fusion was proposed when it was realized that the cold ranges of MeV light ions or GeV heavy ions were of the correct value to drive hollow pellets such that ignition could be achieved in the DT fuel, and also because the deposition physics of electron beams (due to Bremsstrahlung production) was unfavorable. The deposition physics of laser light[48—57] was also giving difficulties as it was found to be anomalous because most of the energy was absorbed at the critical density, leading to the production of hot electrons. However, here the use of shorter wavelengths or higher-energy photons has made the deposition more "classical" since then the absorption mechanism is then mainly inverse Bremsstrahlung. The deposition of both heavy and light ions is expected to be classical.[1,3,9,58—69] This means that no superathermal particles are generated which would lead to preheat. Preheat mechanisms are limited to knock-on ions entering the fuel or $K\alpha$ radiation excited by electrons falling into core states, having previously been excited by an incoming ion.

Much of the research in inertial-confinement fusion is aimed at eventually producing a working commercial reactor.[8—10,22—28,53,56] The main advantages of the use of heavy ions are their favorable range-energy relationship, that permits high kinetic energy ions to be stopped in the outer-shell materials of typical size (7 mm—1 cm diameter) inertial-confinement fusion pellets. As mentioned above the energy deposition is expected to be classical and not to involve collective instabilities or nonlinear effects.[3,69] Secondly, the technology of linear accelerators is well established, and practical accelerators already have the high efficiencies (20—30%) and high repetition rates (10 Hz) necessary for a commerical power plant. Thirdly, there is the favorable scaling of cost versus energy (joules) as target requirements for high gain have reached the multimegajoule level. Because of the heavy mass of heavy ions for a given energy the current is low and the density of ions is small. This allows the use of ballistic focusing. However, the size and cost of such a heavy-ion-beam accelerator even for experimental purpose is very high.[8,9] The pellet design should be as simple as possible so that fabrication is feasible and the cost of the pellet should be as low as possible, preferably a few cents per pellet.

In the light-ion case,[3,15] the deposition physics is again very favorable and the construction of machines is relatively cheap. It is also an energy-rich technology since the energy can be stored in capacitor banks.[70—72] The problem is to deliver this energy in a short enough time (~ 10 ns). This is achieved by loading the capacitors in parallel and discharging in series by closing switches. Even so the pulse length is of the order of 50 ns and must be shor-

tened by the use of plasma-erosion switches,[73,74] inductive compression,[73,74] or by bunching the beam in flight by ramping the diode voltage.

The voltage is led down a transmission line (*Blumlein*) often with the use of magnetic insulation and applied to a diode, pinch reflex, applied B, etc. The diode produces a powerful beam of ions, where the voltage is planned to be up to 30 MeV and the current is of the order of megaamperes. Problems are the complicated pulse shape, the distribution of ion energies, and the contamination with protons if, say, a lithium or deuterium beam is used. Furthermore, the ion density is very high and this means that focusing is difficult. Beam transport to the pellet has to be carried out by the use of plasma channels, precreated by a discharge or by the firing of a laser beam. Transport in narrow plasma channels is more difficult[75] and the diameter necessary is ~ 1 cm.[75] This leads to the need for targets that are at least 1 cm in diameter.

If one is studying basic physics problems, there is considerable freedom in choosing the type of target, but for a reactor design certain constraints have to be satisfied.[3,6–15,25,26] The fractional burnup and the output energy needed determine the amount of DT fuel needed, and the masses and thicknesses of layers have to be adjusted according to the total DT mass. The size of the target must be adjusted to the focusing capability. The total mass of the DT fuel will determine the energy in the pulse, because it needs to be accelerated to $\sim 3\times 10^7$ cm/s in order to reach the ignition temperature after the collapse and compression.

The power level is determined by the acceleration needed to reach this terminal velocity within the distance of collapse (i.e., the radius of the target) and the pulse must have a corresponding length, taking into account the fact that any signal from the end of the range to the inside of the pellet needs a delay time determined by the distance divided by the velocity of sound. The shape of the pulse and in particular the need of a prepulse[3,11–15,76–79] is determined by shock timing and the need to deposit enough entropy in the inner layers of DT to obtain ignition. The prepulse creates a density gradient down which the second shock from the main part of the pulse moves. This leads to selective shock heating of the center of the fuel. Also it is well known that by the use of several shocks a given compression is achieved with less entropy production than is created by one shock. This allows the rest of the fuel to remain on a low adiabat, so that good compression can be achieved. One of the main obstacles in the way of achieving inertial-confinement fusion is the occurrence of the Rayleigh-Taylor instability. This occurs when the low-density heated part of the pusher (Pb-Li or Li) pushes and accelerates by thermal and ablation pressure the compressed part of the pusher. This is basically unstable because the heavier fluid falls into the lighter fluid in the "gravitational field" created by the acceleration. In order to avoid this the pusher should be made thick so that the pushed shell does not break up. However, this costs a lot of energy. The illumination should be very symmetric as should the fabricated target, if this instability is to be avoided.

Previously in numerical simulations[3,11–14,40,43] we have used a relatively simple routine to describe the energy deposition of ions in the outer-shell materials. In particular the range and shape of the profile were fixed and the shape was always a peaked one. Recently we introduced[80] a method whereby the range changed as a function of E, T and ρ (energy, temperature, and density), whereby the range was recalculated in each layer for each time step but with an averaged T and ρ of each layer. In this paper we study in detail the effects of realistic energy deposition on the implosion of reactor-size targets, using a new routine[6,81,82] which uses analytic fits to dE/dR (energy deposition/g) as a function of E, T, and ρ, whereby the energy loss of an ion is calculated in each cell, using the value of dE/dR for the values of E, T, and ρ in that cell.[6,81,82] This allows the nonlinear feedback processes to be calculated[6,81,82] whereby an ion heating the plasma causes changes in T and ρ, which cause in turn a change in dE/dR. dE/dR is calculated for *each* timestep *locally* in each cell up to the end of the range, and in each material. Furthermore, the energy of the incoming ions can be a function of time.[6,81,82] The energy deposition is calculated by the GORGON code[1,3] which is an extension of the work of Nardi, Peleg, and Zinamon.[58] A method of fitting the data analytically has been developed which allows for fast, accurate, and computing-efficient calculation of the energy deposition in the MEDUSA-KA code[3,4,11,14] which is an extended version of the MEDUSA code.[2]

The calculations are carried out on the HIBALL-I (Refs. 3, 11–14, 34,40–42, 76, and 77) and HIBALL-II (Refs. 6, 13, 42, 83) reactor-type pellets. Range shortening which occurs because of transfer of bound to free electrons and also because of the increase of the effective charge in hot plasmas[1,59,60] can be compensated for by ramping (increasing) the incoming ion energy[1,81,82] and by Marshak wave propagation.[6,7,42,43,81–97] The range shortening (especially if the dynamic, plasma-effective charge is included) is so large that ion-energy ramping is probably always desirable, but the amount is dependent on the temperature that the plasma reaches, i.e., the power that has to be used. The power level is fixed by the size of target and the mass of the payload, with reference to the avoidance of instabilities. The efficiency of radiation compensation of range shortening is determined very strongly by the temperature reached and hence by the power level used. Ion-energy ramping is very convenient because it provides an "external dial" with which one can tune the pellet. On the other hand, radiation provides a totally natural mechanism which does not require changes in the ion beam or accelerator design.

The organization of the paper is as follows. In Sec. II A the theory of the energy deposition of heavy and light ions in dense plasmas is discussed. In Sec. II B we present the physical model used in the GORGON code for the calculation of the energy deposition of ions in cold materials and hot dense plasmas.[1] In Sec. III A we describe briefly the MEDUSA code and improvements made in order to carry out these calculations. In Sec. III B we give details of numerical simulations of HIBALL-I (Refs. 3, 11–14, 40–42, 76, and 77) and HIBALL-II (Refs. 6, 13, 42, and 83) type reactor size inertial-confinement fusion targets, and discuss the compensation of range shortening by volt-

age ramping and radiation transport, which proves to be necessary in order to obtain ignition and high gain. It is to be noted that various modifications have been made to the basic HIBALL-II design.[7,42,43,83,6,13] In this paper the "cavity region" made of lithium has been substantially enlarged to obtain a higher gain when radiation compensation for range shortening is used. Also the pusher-fuel instability problem has been ameliorated by the introduction of a low Z, low ρ lithium layer between the radiation shield and the fuel. Detailed results of the simulation of the first modified target is discussed later, and results of the second, including radiation transport in the compression and burn phase including ablation stabilization of the hydrodynamic instabilities (in the compression phase) are discussed in Refs. 7, 43, 85, 86, and 91). In Sec. IV A we present an analysis of the Rayleigh-Taylor instability during the compression phase and its amelioration by density-gradient and ablation effects. In Sec. V A we present some theoretical considerations on the ablation, compression, ignition, and burn and inertial-confinement-fusion targets. Section V B contains our conclusions.

II. THE STOPPING POWER OF IONS; THEORY AND SIMULATION

A. The theory of energy deposition of heavy and light ions in hot dense plasmas

Most of the critical issues present in laser fusion[48–57] are also valid for ion-beam fusion except for the different energy-deposition physics. The laser energy deposition is highly nonlinear and occurs mainly at the critical density. The ion energy deposition occurs via a multitude of small energy transfers occurring at each ion-electron collision. Maximum energy transfer occurs when the ion velocity is the same as the average electron-excitation energy. Above and below this energy or velocity the energy loss drops off quite rapidly.[1,3,58–67]

We now discuss some approaches that have been made by various authors to the calculation of energy loss in hot plasmas, making reference to the theory in cold materials where necessary. The normal approach taken is to divide the electrons in the partially ionized plasma into free and bound electrons and then to calculate the stopping power of each set of electrons separately. This approach has been criticized by Breuckner *et al.*[98] who assumed instead of additivity of the stopping power, additivity of the dielectric function for the bound and free electrons. However, the calculation then proceeded to use a rather simplified form of the dielectric function for both bound and free electrons and to include collisions in a way that does not satisfy the sum rules.[99–101] Returning to the usual method [while noting that a combination of a sophisticated treatment of the dielectric function together with summation over all states (free and bound) would be more desirable] the number of free and bound electrons is normally calculated[1,3,58,62,63] either within the Saha model (which does not apply to dense plasmas) or using the Thomas-Fermi model.[1,3,57,102–105] The stopping power of the free electrons is calculated using the dielectric-function theory[1,106–111] or the classical plasma-theory approach[1,112–114] originally due to Chandrasekhar[112,113] and described by Spitzer[114,115] whereas the contribution from the bound electrons is calculated using the Bethe,[116–117] Bohr,[118–122] or Bloch theory.[123–125] The average excitation energy I used in the Bethe theory is calculated either using the Thomas-Fermi theory[1,3,58,103–105] using relativisitic self-consistent Hartree-Fock atomic theory or by calculating the electron density using methods used in solid-state physics.[63] Details of the model used in the calculations described in this paper are given in Sec. II B.

The first calculations of the energy loss of ions carried out specifically for ion fusion were done by Bangeter[126] and Mosher.[127] Finite-temperature plasma effects were included by Nardi, Peleg, and Zinamon.[1,3,58] Deutsch and Long[128–130] have calculated the dielectric function at finite temperatures and have shown how to include partial degeneracy in stopping-power calculations. The main results is that the stopping power per electron decreases as the plasma becomes nondegenerate. Mehlhorn[62,63] has carried out calculations using methods similar to Zinamon *et al.*[1,3,58] and to us[1,3,65–67] but with a scaled calculation of the Bethe parameter and a classical plasma-theory approach to the loss by free electrons. Mehlhorn recently has tried to include better atomic physics and to calculate with real electron densities.[63] The calculations are, however, somewhat inconsistent in that the Saha equation is still used to calculate the number of free and bound electrons. More[60] has used a Thomas-Fermi approach whereby the dielectric-function theory has been used for the electron charge density (both free and bound) within the sphere of each pseudoatom. Sayasov[100,131,132] has pointed out that these plasmas are actually nonideal, for instance, partially ionized lead at solid density and 200 eV has a coupling parameter $\Gamma = 1.3$. He has attempted to calculate these effects when the nonideality is weak in fully ionized plasmas.[100] He has also emphasized the role of ion-ion correlations.[132]

Besides the plasma effects involved in the stopping power of bound and free electrons and those involved in the calculation of the Bethe I parameter (due to electron-excitation effects), the effective charge is also strongly dependent on the plasma properties.[59,60] This has been calculated by Zinamon *et al.*[59] and by More *et al.*[60]. It has been found to be a very important effect, and to lead to additional range-shortening effects by up to a factor of 2 at lower energies. At high energies there is not much change because the ions are highly stripped. The difference between the "cold" effective charge and that in the hot plasma is due to the fact that recombination is easier via bound electrons than via free electrons. Detailed calculations of energy-loss profiles for heavy-ion fusion have been carried out by Long and Tahir,[1,3,65–67] by Breuckner *et al.*,[98] and, using simpler methods, by Meyer-ter-Vehn and Metzler.[68] Mehlhorn[62,63] and More[60] have also carried out detailed calculations for light and heavy ions, and Beynon[61] has also carried out investigations of ion-energy deposition for ion-beam fusion.

In general, results obtained are qualitatively similar but different physics can lead to up to 30% changes in dE/dR for certain energy ranges. Results are, however, clearly very sensitive to the effective charge used. One

very notable difference is that some authors have found range lengthening as well as range shortening in certain regions of parameter space, but have proposed different mechanisms for this. For instance, Breuckner *et al.*[98] found range lengthening at lower temperatures especially for heavy ions. They suggested that this was due to free-electron—bound-electron collisions. Basko[133] found that for Bismuth ions in lead, at densities $\sim 10^{22}$ atoms per cm^3, the range first increases with temperature by 10—40% and only then begins to drop. This was attributed to the increase of ionization with temperature which has a twofold effect on the stopping power. On the one hand, higher values of the Coulomb logarithm for free electrons as compared to bound electrons increases the stopping power. On the other hand, the increase in the number of free electrons increases the plasma frequency w_p and the mean excitation energy I increases so that both the Coulomb logarithms decrease leading to a decrease in the stopping power. This effect is due to the partial removal of electrons screening the electric field of the nucleus. However, these effects are included in the GORGON code[1] where they have not been detected, at least at solid densities. More investigation of these points is needed. Certainly at high densities where there is considerable pressure ionization, little change in the range would be expected, until a temperature is reached at which thermal ionization starts. At solid density this is noted in the GORGON code.[1] One should note that at high temperatures the range does start to increase again because the ion velocity becomes less than the thermal velocity of the free electrons.

It has also been noted above, that the range should increase due to the removal of degeneracy. This may be quite important in the analysis of the energy-loss experiments that have been carried out.[20—23] In particular, experiments have been carried out for the stopping power in aluminum plasmas.[20] In aluminum metal the three *sp* electrons form a hybridised band[134,135] and are quasifree conduction electrons with little enhancement in their effective mass.[135] The stopping power of these electrons should be and is treated using the dielectric-function-theory approach for a nonideal (strongly correlated) plasma taking into account plasma effects. Further, the Fermi energy is ~ 11.6 eV and so degeneracy effects must also be considered within the conduction band. Of course, as soon as the plasma is heated above the melting point even the lattice loses its periodic order but bands are still found to exist in disordered systems.[136—138] According to Deutsch[128,130] the energy loss should decrease as the degeneracy is lost, which would predict an initial range lengthening in aluminum. The calculations did not include the effect of nonideality. In Refs. 22, 23 and 84 we have given a detailed analysis of the low-energy stopping power (~ 1.6 MeV) of protons in aluminum. We have discussed the attempt of Young *et al.*[20] to measure the increase in the stopping power or the decrease in range with temperature. However, in Refs. 22, 23 and 84 we pointed out that due to the expansion of the foil much of the range shortening is due to the decrease in the density. In fact, we showed that this problem in one dimension can be solved exactly (analytically) and the density profile achieves a Gaussian (probability) functional form, while the temperature is constant, after a short characteristic time.[22,23,84]

B. The GORGON computer code (Ref. 1) for the numerical calculation of the energy deposition of ions in cold materials and hot dense plasmas

In order to simulate numerically the energy deposition of ions in spherical, hollow, multilayer pellets or plane targets one must first be able to calculate the energy deposition of ions in plasmas from densities of $10\rho_s$ (ρ_s is solid density) to $\rho_s/100$ and temperatures from 0 to 500 eV. Secondly, one must be able to couple the results into a hydrodynamic pellet code in an accurate, computing-efficient manner. The GORGON code[1] accomplishes the first task, a method of achieving the second is described in Ref. 7, and the MEDUSA code[2—7] is used to describe the hydrodynamic motion of the plasma and other physical effects such as equation of-state (EOS), conduction, nuclear burn processes, etc.

The GORGON energy-deposition code[1,3,58] is based on a code written for protons by Nardi, Peleg, and Zinamon[58] which has been extended[1,3,139—142] to treat other problems such as charged particles in DT and heavy ions by including some other physical effects. An ion[1,3] travelling through a charged plasma loses energy mainly to electrons by a series of small-angle collisions. In each individual collision the amount of energy lost is very small, but because of the long range of the electrostatic forces, there are very many such collisions, so that the total loss is large. From the point of view of transport theory a Fokker-Planck equation[143—148] can be used to describe the transport of ions in a plasma including both a slowing-down term and small-angle collisions. However, since the mass of the ion is much larger than that of an electron, a fast-moving ion ($v_I \gg v_e$), with a velocity much greater than the thermal-electron velocity, is deflected through very small angles, and one can consider that the ion travels in a straight line (cf. charged particle tracks in a cloud chamber with no applied magnetic field). The projectile ion is considered to be a point charge with specific mass, energy, and charge, the last two being time dependent. In the version of the code used for these calculations the plasma is considered to be ideal and degenerate or nondegenerate according to whether the temperature is above or below the Fermi temperature.

The physical model used in the calculation distinguishes between free and bound electrons in the target. In strongly coupled plasmas where no clear distinction between free and bound electrons exists, the degree of ionization may be thought of as a parameter separating the range of applicability of two asymptotic models for the electron-excitation spectra. The energy-loss processes are essentially divided into free-free, bound-bound, and bound-free transitions, just as in opacity calculations.[149—151] The contribution of the bound electrons to the stopping power is calculated according to Bethe's theory,[1,3,116,117] taking account of the difference in characteristic excitation energies between a neutral atom and a plasma ion via the Thomas-Fermi theory. The con-

tribution of the free electrons is calculated using the dielectric-function theory for a nondegenerate plasma using numerical integration with a more simplified (analytic) evaluation being used if the electrons are degenerate.

In the model used in this calculation knowledge of the average degree of ionization in the plasma is required because of the separate treatment of bound and free electrons. This is calculated using the Thomas-Fermi model of the atom at finite temperature. For this purpose the Thomas-Fermi model is solved using the method described by Latter,[152] which yields values for the electron-density distribution in the atomic sphere $n(r)$ for a given density and temperature of the target material, as well as the potential $V(r)$ and the chemical potential μ. The number of bound electrons which yields the average degree of ionization is given in the Thomas-Fermi model by

$$N_b=\frac{32\pi^2}{h^3}\int_{-\infty}^{0}dE\frac{1}{\exp(E-\alpha)/k_BT+1}\times\int_0^{r(E)}m\{2m[E+eV(r)]\}^{1/2}r^2dr\ , \tag{1}$$

where E is the total electron energy, m is the electron mass, T is the temperature, k_B is Boltzmann's constant, h is Planck's constant, and $r(E)$ is the radius which satisfies the condition

$$eV(r(E))=-E\ , \tag{2}$$

i.e., where the kinetic energy of the electron just equals its potential energy. From the number of bound electrons, the number and density of the free electrons are determined and used in the calculation of the stopping power due to the plasma free electrons. The calculated structure of the ions is used to determine the bound-electron contribution to the stopping power.

The contribution of bound electrons to the stopping power is calculated by Bethe's theory[1,3,116,117] including corrections due to the differences betwen a plasma ion and a neutral atom. The basic physical parameter is the average excitation energy I, defined by

$$\ln I=\frac{1}{N}\sum_i\ln(\hbar\omega_i)\ , \tag{3}$$

where N is the number of bound electrons participating in the slowing-down process and $\hbar\omega_i$ are the characteristic excitation energies. In these calculations the ω_i's are interpreted as the frequencies of revolution, following Bohr's model.[118,119] In order to calculate I within the framework of the Thomas-Fermi model one notes that at each radius r a spectrum of revolution frequencies is determined by the Fermi energy distribution at this radius,

$$\omega(r)=\{(2/m)[E+eV(r)]\}^{1/2}/r\ . \tag{4}$$

Here E is the total electron energy. The number of electrons per unit frequency having a revolution frequency ω is

$$n(\omega)=(32\pi^2\omega^2m^3/h^3)\times\int_0^{r_{\max}(\omega)}r^5(\exp\{[\tfrac{1}{2}m\omega^2r^2-eV(r)-\alpha]/k_BT\}+1)^{-1}dr\ . \tag{5}$$

Here $r_{\max}(\omega)$ is the radius beyond which the energy that corresponds to ω yields a free electron, i.e.,

$$eV(r_{\max}(\omega))=-E\ . \tag{6}$$

The effective excitation energy is given, within the framework of this model, by

$$\ln I=\frac{1}{N}\int_0^\infty n(\omega)\ln(\hbar\omega)d\omega\ . \tag{7}$$

A shell correction is included in the calculation by eliminating from the integration in Eq. (7) those electrons for which

$$2mv^2<\hbar\omega\ , \tag{8}$$

where v is the projectile velocity. The solution of the Thomas-Fermi model provides the required values of $V(r)$ (the potential), μ (the chemical potential) and $n(r)$ (the electron density) required in the above integrations.

The free-electron contribution to the stopping power is calculated using the plasma-dielectric theory.[106,153–157] The energy loss is given by

$$\frac{dE}{dR}=-\frac{2e^2Z_{\rm eff}^2}{\pi\rho}\int_0^\infty dk\,k\int_0^1 d\mu\,\mu\,\mathrm{Im}\left[\frac{1}{D(k,\omega=k\mu v}\right]\ , \tag{9}$$

where ρ is the density, $R=\rho x$ is a distance into the material, v is the projectile velocity, k is the wave number, $\mu=\cos\theta=\mathbf{k}\cdot\mathbf{v}/|\mathbf{k}||\mathbf{v}|$, D is the dielectric function of the plasma and ω is the frequency. In calculating the dielectric function a classical, nondegenerate plasma is assumed, and collisions in the plasma are taken into account. The collision time is given by

$$\tau=3m^{1/2}(k_BT)^{3/2}[4(2\pi)^{1/2}e^4Z_{\rm eff}n\ln\Lambda]^{-1}\ , \tag{10}$$

where n is the free-electron density, $Z_{\rm eff}$ is the average ion charge, and $\ln\Lambda$ is the Coulomb logarithm. The dielectric function is given by

$$D(k,\omega)=1+2x^2[1+xZ(\zeta)]\omega_p^2/\omega^2\ , \tag{11}$$

where $\xi=x+iy$, $Z(\xi)$ is the plasma-dispersion function, $x=\omega/kV_t$, $y=\nu/kV_t$ is the collision frequency, V_t is the free-electron thermal velocity, and $V_t=(2k_BT/m)^{1/2}$. An upper cutoff wave number is used in the integration in Eq. (9) following Bethe,[116,117]

$$k_c^{-1}=e^{-\gamma}\hbar/mV_t\ , \tag{12}$$

$$\gamma=0.5772\ . \tag{13}$$

The code contains a calculation of the energy loss to degenerate electrons. This follows the approximate evaluation of the stopping power within the dielectric-function formulation for a totally degenerate electron gas given by Ritchie.[158–161] This is important because in aluminum, for instance, the outer three *sp* electrons in the solid form a hybridized conduction band. These electrons behave like free electrons with an increased effective mass[134,135] due to the interaction with the core potentials. Effects due to the nonideality of the plasma ($r_s\sim2$–5 in metals) should also be included. Further, in highly compressed DT in pellet simulations[3,6,7,11–14] most of the DT remains

on a low adiabat. At a high density such as 600 g/cm^3, the Fermi energy is 1 keV, and actual temperatures are approximately 600 eV. α particles created during central ignition and propagating burn[151–153] stream out into this degenerate material and hence one needs to be able to calculate the range or dE/dR (Refs. 162–166) in degenerate plasmas, and nuclear scattering is treated in Refs. 164 and 167.

If $\varepsilon_F > k_B T$ the code calculates the stopping power in the following way. For V_I (ion velocity) $> V_F$ (the Fermi electron velocity),

$$\frac{1}{\rho}\frac{dE}{dx} = \frac{-Z_{\text{eff}}^2 e^2 \omega_{\text{pl}}^2}{\rho v_I^2} \ln\left[\frac{2mv_I^2}{\hbar\omega_{\text{pl}}}\right], \tag{14}$$

where ω_{pl} is the plasma frequency, dE/dx is the energy loss per unit distance travelled, Z_{eff} is the effective charge, and e is the charge on the electron.

If $V_I < V_F$,

$$\frac{1}{\rho}\frac{dE}{dx} = \frac{-2}{3\pi}\frac{Z_{\text{eff}}^2 e^4 m^2 v_I}{\hbar^3 \rho} 2\ln\left[\frac{2mv_F^2}{\sqrt{3}\hbar\omega_{\text{pl}}}\right], \tag{15}$$

where V_F is the Fermi velocity. Skupsky[165] and Arista and Brandt[166] have given treatments valid for partial degeneracy, when $V_I < V_F$. Deutsch *et al.*[128] has given a much more complete and accurate evaluation, see also Refs. 168 and 169.

For low velocities, ion scattering becomes important and this has been included following Mehlhorn.[62] The effective charge used is[170]

$$Z_{\text{eff}}(V)/Z_0 = [1 - 1.034\exp(-137\bar{V}_r/Z_0^{0.69})], \tag{16}$$

$$\bar{V}_r = V_r/c, \quad V_T = (V_t^2 + V_I^2)^{1/2}, \tag{17}$$

where V_T is the electron thermal velocity, Z_0 is the atomic charge of the ion, and c is the velocity of light.

The effective charge in hot plasmas is thus somewhat greater than in cold materials, especially at lower energies. This effect is still somewhat underestimated as shown by more detailed microscopic calculations based on the solution of rate equations and atomic physics calculated using a self-consistent relativistic Hartree-Fock method.[59,60] For the slowing down of α particles in DT, nuclear scattering has been included.[142,164]

In Fig. 1 we show dE/dR plotted against R (in units of mg/cm^2) for 10-GeV bismuth ions in solid density lead and in Fig. 2 we show the range versus temperature. Range-shortening effects due to the transfer of bound to free electrons or the excitation of electrons to higher states due to the rise in temperature are evident. Also there is a sharpening in the deposition profile due to the increase in the effective charge at low energies. This effect would be more pronounced if a dynamic effective charge in the hot plasma was used as calculated in Refs. 59 and 60. Similar results are given for bismuth ions in lithium in Figs. 3 and 4. For bismuth ions in lead the contribution to the stopping power due to bound and free electrons at three temperatures is given in Fig. 5. This clearly shows how the bound-electron contribution to the stopping power dominates at low temperatures and how the free-electron stopping power dominates at 1 keV. The results for the stopping power of protons in aluminum are discussed in Refs. 22 and 23. The results for α particles, deuterium, and tritium ions in deuterium-tritium mixtures at temperatures and densities typical of the burn phase of an inertial fusion pellet are presented in Ref. 164. The method of coupling of energy deposition into the MEDUSA code has been described in Ref. 7. Some examples of the interpolation procedure are given in Ref. 6.

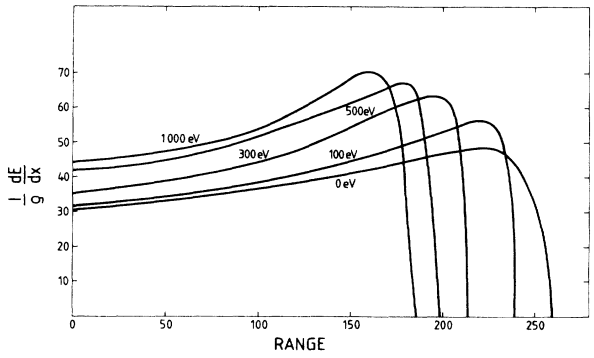

FIG. 1. Energy loss of 10-GeV Bi ions in solid-density lead at temperatures from 0 to 1 keV. Units: range, mg/cm^2; energy deposition, 10^6 keV cm^2/g.

III. THE SIMULATION CODE AND RESULTS OF THE NUMERICAL SIMULATION OF ION-BEAM-DRIVEN REACTOR-SIZE INERTIAL-CONFINEMENT-FUSION TARGETS, DURING THE IMPLOSION, IGNITION, AND BURN PHASES

A. The MEDUSA code (Refs. 3–5 and 11) and the extended MEDUSA-KA (Refs. 3, 5, and 11) version for ion-beam fusion

The MEDUSA code was written and published as MEDUSA-I (Ref. 2) to describe the compression and burn of deuterium-tritium solid spheres illuminated by laser light. It was written in the Olympus format[2] which provides a general framework into which various routines describing different physical processes can be inserted. The original version of the code has been modified and

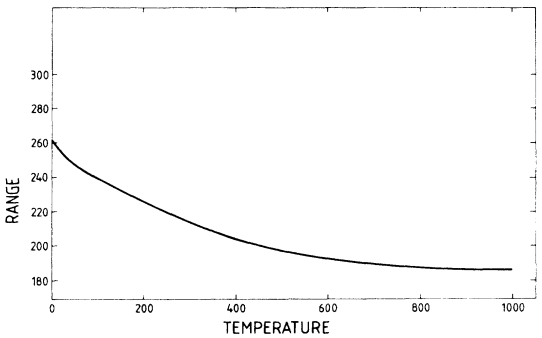

FIG. 2. Range of 10-GeV Bi ions in solid-density lead plotted as a function of temperature. Units: range, mg/cm^2; temperature, eV.

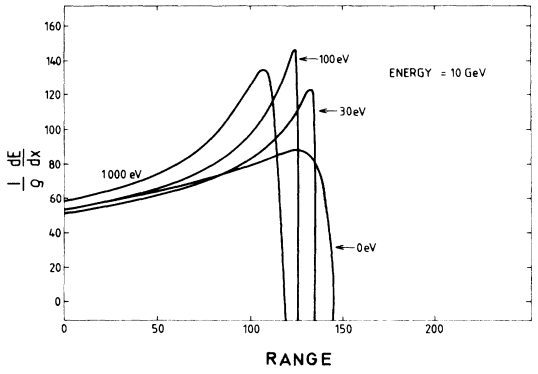

FIG. 3. Energy loss of 10-GeV Bi ions in solid-density lithium at temperatures from 0 to 1 keV. Units as in Fig. 1.

some of these modifications are documented in detail in Refs. 3 and 5. The code is a one-dimensional Lagrangian hydrodynamic code, where the hydrodynamic motion is described by the Navier-Stokes equation,

$$\rho d\mathbf{u}/dt = -\nabla P \ , \tag{18}$$

where $\mathbf{u}=d\mathbf{r}/dt$ is the velocity, P is the total pressure, and ρ is the density, and shock motion is described by an artificial viscosity and a viscous-pressure term.[171] The code treats ions and electrons as separate thermodynamic subsystems and calculates the temperature of ions and electrons using two temperature equations of the form

$$(C_v)\frac{\partial T_i}{\partial t}+(B_T)_i\frac{\partial \rho}{\partial t}+P_i\frac{\partial v}{\partial t}=S_i \ , \tag{19}$$

where i represents electrons, ions, or radiation; T_i is the respective temperature; and P_i the partial pressures

$$(C_v)_i=\left[\frac{\partial u_i}{\partial T}\right]_\rho \text{ and } (B_T)_i=\left[\frac{\partial u_i}{\partial T}\right]_\rho \tag{20}$$

are the specific heat and compressibility as determined by the equation of state (EOS).[3,11,172–174] The S_i's stand for the source term.

For ions

$$S_i=H_i-K_{ie}+Y+Q \ , \tag{21}$$

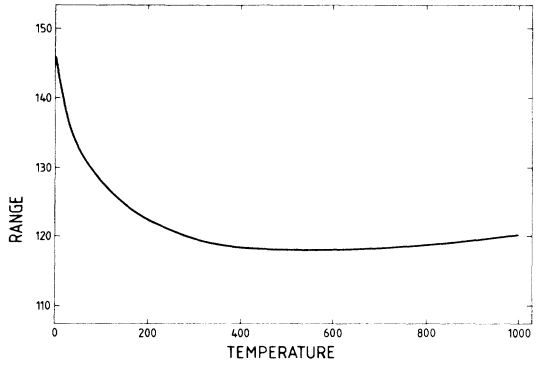

FIG. 4. Range of 10-GeV Bi ions in solid-density lithium plotted as a function of temperature. Units as in Fig. 2.

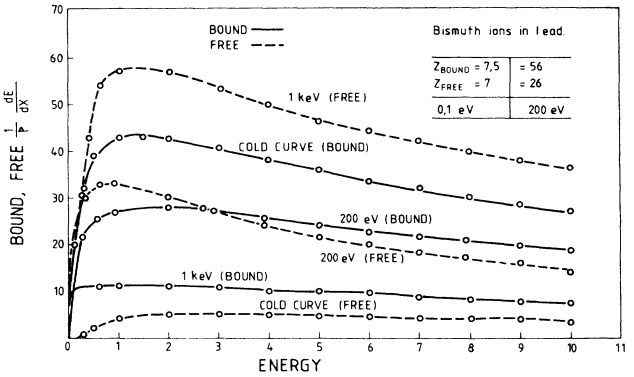

FIG. 5. Energy loss to free and bound electrons in cold materials and hot dense plasmas as illustrated by Bi ions in solid-density lead at 0 eV, 200 eV, and 1 keV. Units: energy, GeV; energy deposition as in Fig. 1.

where H_i is the thermal conduction due to ions, K_{ie} is the electron-ion exchange term, Y_i is the nuclear burn rate, and Q is the viscous heating.

$$S_e=H_e+K_{ie} \ , \tag{22}$$

where H_e is the conduction due to electrons and radiation.[175] This physical model and the modifications made to the code which were necessary to include radiation effects in a radiation conduction approximation are described in detail in Refs. 6, 7, 42, 43, 76, 77, 85–87, and 91, where

$$H_e=\rho^{-1}\nabla\cdot K\nabla T \ , \tag{23}$$

$$K=K_e+K_r \ , \tag{24}$$

$$K_e=1.8\times10^{-10}T^{5/2}(\ln\Lambda)^{-1}\bar{Z}(\bar{Z}^2)^{-1} \ , \tag{25}$$

$$K_r=(16\sigma/3)l_R T^3 \ , \tag{26}$$

and where the other thermodynamic variables such as specific heat, compressibility, and pressure have been modified to include the radiation contribution.[7] Also K_e is the electron conductivity, K_r is the radiation conductivity, Λ is the Coulomb logarithm, $\bar{Z}$ is the average degree of ionization, $\bar{Z}^2$ is the average of the square of the degree of ionization, σ is Stefan-Boltzmann's constant, l_R is the Rosseland mean free path, and c is the velocity of light.

The specific heat, compressibility, and pressure are all modified correspondingly for the effect of radiation. Radiation conduction affects the propagation of shock waves and produces characteristic Marshak waves.[6,7,23,83,85,88–97] The speed of propagation of Marshak waves for various boundary conditions has been successfully compared to analytic solutions.[23,83,84] Both radiation and electron conduction are flux limited, and in long mean-free-path situations the radiation conduction is flux limited by emission coefficients.[7,85–87]

The code has also been improved to take account of radiation as a separate temperature, namely, a three-temperature model. These modifications have been described in Refs. 4,176,177.

The equation of state is a corrected Thomas-Fermi model,[172–174] fitted by analytic formulas to Los Alamos

EOS data.[3,11,172] The ionization routine can be Saha or Thomas-Fermi depending on the density of ions. The Saha equation is valid for a gas of intermediate density, say $10^{14}-10^{18}$ atoms/cm^3. The Thomas-Fermi model is better when pressure ionization comes into play due to overlap of atomic orbitals.[60] The plasmas in ion-beam fusion are usually so dense that the Thomas-Fermi model is a better model for ion-beam fusion. The energy-deposition model is described in Sec. II B and is based on the Thomas-Fermi model as well. The code has hence a physically consistent model for EOS, ionization, and ion energy deposition. It also uses a simple but globally correct escape-fraction treatment of nonlocal α-particle energy deposition.[164] This method shows that about 20% of the energy of the α particles escape the fuel agreeing macroscopically with more sophisticated treatments[178,179] and with analytic estimates.[141] The range-temperature curves in Ref. 164 include the energy loss due to ions and electrons (nuclear scattering has also been included Fig. 13) and are calculated using the GORGON code. Degeneracy effects are included in the electron energy loss when $k_B T < \varepsilon_F$. This causes the α particles to stop very quickly in the cold degenerate fuel surrounding the burning-propagation phases. The electrons in the highly compressed lead tamper are also degenerate when it is cold. The various processes included in the compression phase are shown in Fig. 6, and the processes in the burn are shown in Fig. 7. The only processes not included in the code are the neutron transport in the burn[180] and the effect of the energy loss of the knock-on ions which they produce. All these effects can be included by an escape-probability technique[164,180] or the escape-fraction technique[141,164] among others.

The void is filled with DT at a vapor pressure of 14 K, although the burn in this region is turned off. There are two reasons for using this inner-boundary condition. The first is that in a reactor scenario pellets are fired into the reactor chamber at 4 K, but the radiation and friction heating of the background gas are so great that even in the short time taken to reach the center of the chamber (~ 1 msec) the inner boundary of the DT heats up to 14 K in the heavy-ion case.[8,181] The situation could be even more serious for the light-ion case because the gas in the reactor chamber is at a higher density (because it has to support beam transport in a preformed plasma channel).[181] Secondly, the first shock will heat the DT inner surface up to 10 eV, setting it in motion. Molecular evaporation[182–184] will then take place into the void with a time constant given by t_{evap},

$$t_{\text{evap}}^{-1} = \alpha_v (A/V)\sqrt{(k_B T/2\pi M)} , \tag{27}$$

where A is the area ($4\pi R_0^2$), V is the volume ($\frac{4}{3}\pi R_0^3$), M is the mass of the DT ion, k_B is Boltzmann's constant, and T is the temperature (surface). The vapor pressure is given by an expression of the form,[185,186] see Fig. 8,

$$\ln P_s = \frac{-A}{T} + B \ln T + C , \tag{28}$$

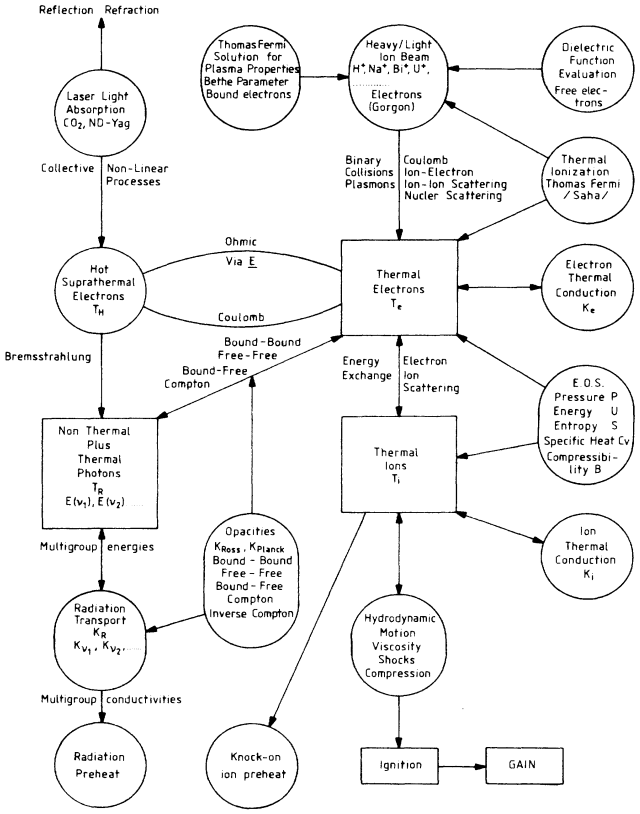

FIG. 6. Important physical processes in the ablation and compression phases of inertial-confinement-fusion targets.

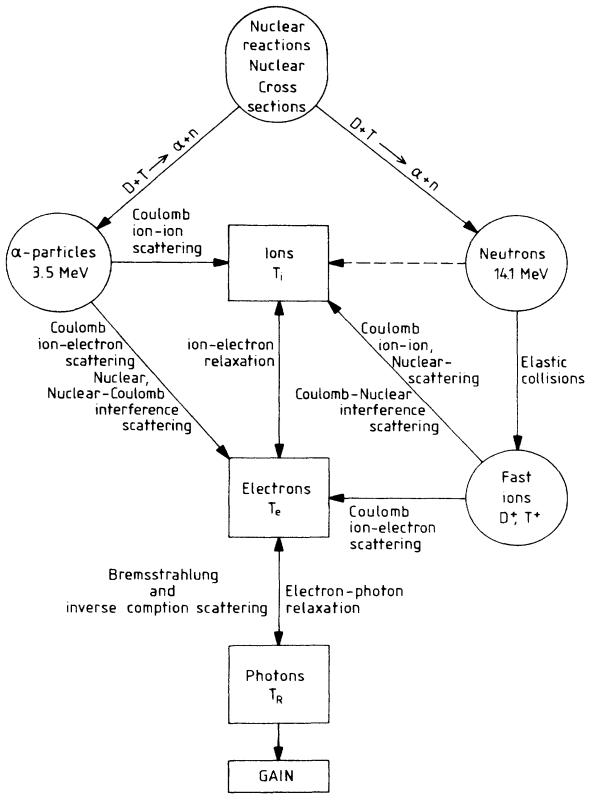

FIG. 7. Important physical processes in the burn of an inertial-confinement-fusion target.

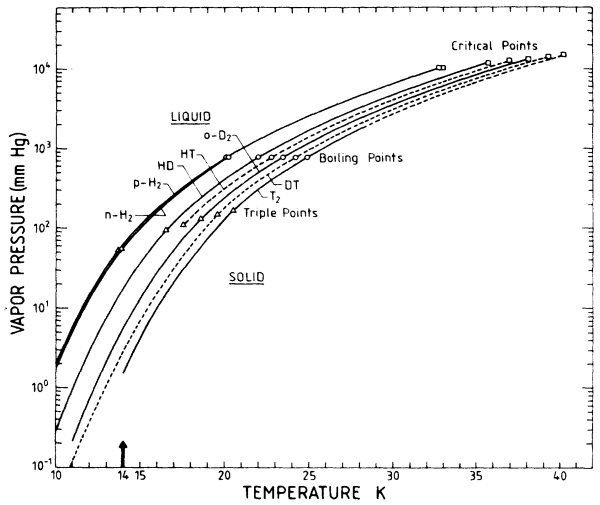

FIG. 8. Saturated vapor pressure of DT plotted against temperature.

where A, B, and C are constants, and P_s is the saturated vapor pressure. The time to reach a pressure where the mean free path is of the order of the void diameter is short compared to the pulse length. The code (which is hydrodynamic) does not calculate this process as (this is a problem in rare-gas dynamics necessitating the use of the Boltzmann equation[186–189] but one can simply put a gas pressure in the void initially. This plays no role in the calculation until near void closure, where the back pressure can reduce compression. At a vapor pressure greater than that at 18 K, this starts to reduce the gain.[6,7,80,85]

The code calculates with an improved DT cross section of the form[190,191]

$$\langle \sigma v \rangle_{\mathrm{DT}} = 9.10^{-22} \exp\left\{ -0.476 \left[\ln\left[\frac{T}{69} \right] \right] \right\}^{2.25} , \qquad (29)$$

where $\langle \sigma v \rangle_{\mathrm{DT}}$ is in $\mathrm{m^2\,s^{-1}}$ and T is in keV, and calculates the usual nuclear reactions.[2]

B. Numerical simulation of reactor-size targets. Results of realistic energy deposition in HIBALL-I and HIBALL-II -type reactor designs, and its compensation by voltage ramping and radiation transport

The coupled version of the GORGON-MEDUSA code described in Secs. II and III has been used to calculate the HIBALL-I (Refs. 3, 6, 11–14, 40–42, 76, 77, and 81) and HIBALL-II (Refs. 6, 7, 43, 82, 86, and 87) -type reactor-target designs. The purpose was to investigate the effects of the inclusion of more realistic energy deposition[192–194] in the pellet calculations as compared to those previously performed for the HIBALL-I and HIBALL-II -type targets. A comparison of energy deposition calculated by the GORGON code and experimental results is given in Table I. The other purpose was to find ways of restoring the gain to an acceptable level if as expected[14] the gain went to zero as range shortening occurred due to the increase in the payload mass which makes the achievement of the requisite payload velocity needed for ignition impossible without increasing the input energy. Calculations performed for plane targets to investigate the compensation of range shortening by radiation are reported in Refs. 84, 85, 7, and 23.

The target designs are shown in Figs. 9 and 10 and the pulse shape used in both cases is the same and is shown in Fig. 13, Ref. 13. The prepulse[11–14] has a relatively low power of a few TW and so the material is only heated to about 10–20 eV during this time. Thus there is relatively little range shortening up to this time. One can see in Fig. 11 that the high-density part of the payload has already formed, the density being much higher in this region than in the other part of the Li-Pb or lithium as the case may be, whereas the temperature is very low. In this region at 14 ns the temperature is 5.4 eV and the electrons in the Li-Pb—Li target are partially degenerate. The plasma is also a nonideal plasma at this point. Therefore it is clear that these effects should be included in the energy-deposition calculations.

From 21 ns on there are two types of calculations to discuss. In the first case we continue with the given ion pulse and allow the range shortening to run its course, and allow compensation by radiation. In the second case the energy of the incoming ions is increased linearly (Fig. 12). The initial energy of the ions (Bi) in the case of the HIBALL-I target is 8.6 GeV, and this is increased linearly in time to 10.9 GeV from 21 to 28 ns. In the case of the HIBALL-II target the initial energy is 8 GeV rising to 10.3 GeV. In the case where the ion energy is ramped the power of the main pulse is 650 TW whereas 500 TW was used before for HIBALL and is still used when there is no ion-energy increase.

We show in Fig. 13 the energy deposition in the pellet with and without ramping of the ion energy at 25.4 ns, for the HIBALL target. In the second case (without ramping) the ion enters the lithium-lead layer with only 2.77 GeV, whereas in the first case the ions enter the lead layer with an energy of 10.2 GeV (not 8.6 GeV) and by the time they reach the lithium-lead layer they have an energy of 4.4 GeV. This allows them to penetrate to more or less the same point as they did at the beginning of the simulation.

In Fig. 14 we show the simulation results for the case

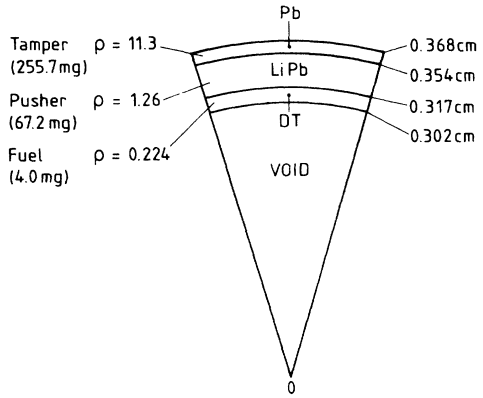

FIG. 9. Schematic diagram of the HIBALL-I target, and target initial conditions with densities given in $\mathrm{g/cm^3}$.

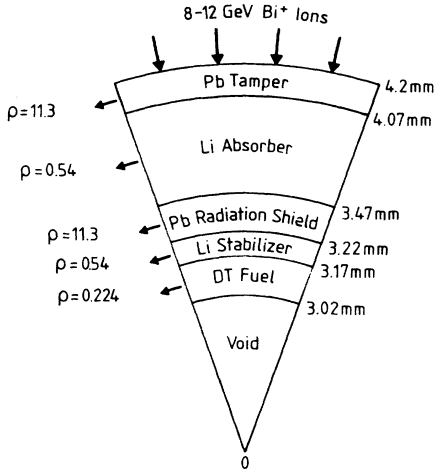

FIG. 10. Same as in Fig. 9 for HIBALL-II target.

where there is no voltage ramping, in the Li-Pb and Pb region, the other cells being DT and the central fill gas. By this time the range has shortened considerably because the temperature has risen sharply when the main (500—600 TW) pulse is applied. The temperature has risen to about 200 eV and it remains around this value. Constant-range peaked depositions used previously tended to produce a higher temperature at the end of the fixed range. This can lead to the generation of faster-moving Marshak waves than is really the case, which move too far in a given time.

As the range decreases and is compensated for, the energy is deposited fairly uniformly in the whole pusher, so that the temperature in this region is fairly constant. The high-density part of the pusher (in the case without ramping) contains much more mass and there is a shallower density gradient on the pushing side especially in the case without ramping. This leads to an improvement in the Rayleigh-Taylor-instability growth rate (see Sec. IV). In Fig. 15 we show the results with ramping. In both cases the original cold range is marked by the first arrow and the actual range at 25.4 ns is shown by the second arrow.

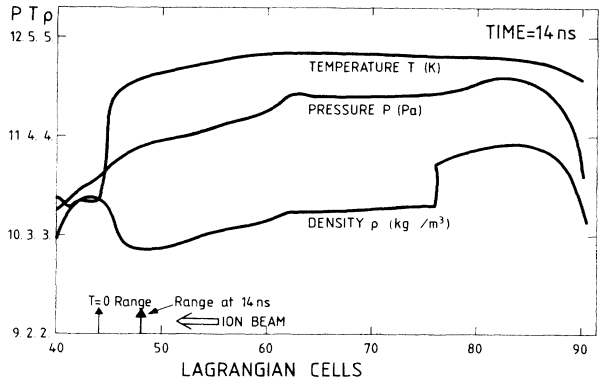

FIG. 11. Implosion of the HIBALL-I target with realistic energy deposition at 14 ns, without radiation, showing range shortening. The ordinate scale is $\log_{10}$.

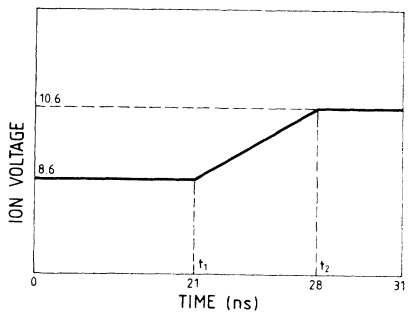

FIG. 12. Energy of ions as a function of time. The ion voltage is given in GeV.

The temperature rises to about 250 eV and as remarked above is fairly constant throughout the pusher. The density gradient is still less sharp than the case where the range is kept (artifically) constant and hence the stability is improved. It should be noted that both radiation and ion-energy ramping can compensate for range shortening. However, the effects are not additive and if the ion-deposition ablation wave moves faster than the Marshak wave, then the radiation does not play much of a role. It will then slightly reduce the ramping energy needed. The velocity of the Marshak wave is given by[6,7,42,43,81–97]

$$\frac{dR}{dt}=\left[\frac{\rho^2 a l_R c T^3}{2.28 C_v t}\right]^{1/2}, \tag{30}$$

where t is the time, $a=4\sigma/c$, σ is the Stefan-Boltzmann constant, l_R is the Rosseland mean free path, T is the temperature, C_v is (specific heat)/cm^3, R is the Lagrangian variable ρx, and c is the velocity of light.

In the case of the ion-beam ablation wave,

$$R(E)=AE^{\alpha}, \tag{31}$$

where A is a constant dependent on temperature and density [(see Ref. 7)],

$$E(t)=E(0)+\frac{\Delta E(t-t_1)}{(t_2-t_1)}, \quad t_1<t<t_2 \tag{32}$$

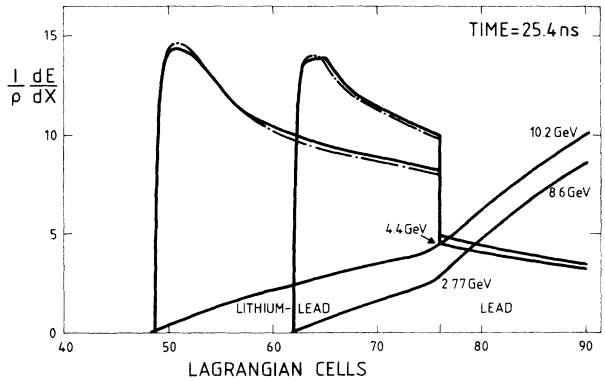

FIG. 13. Energy deposition and ion energy in HIBALL-I target with and without ion-energy increase, showing range shortening at 25.4 ns.

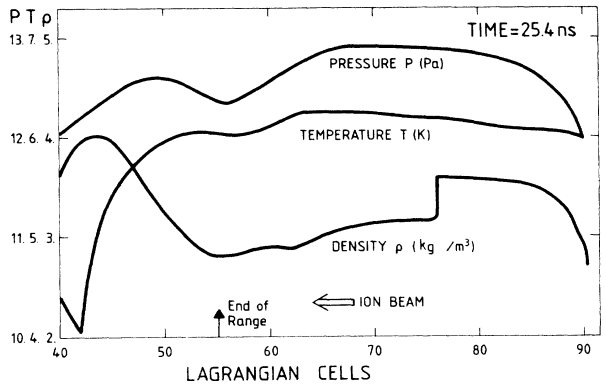

FIG. 14. Implosion of a HIBALL-I target without ion-energy increase at 25.4 ns. The ordinate scale is $\log_{10}$.

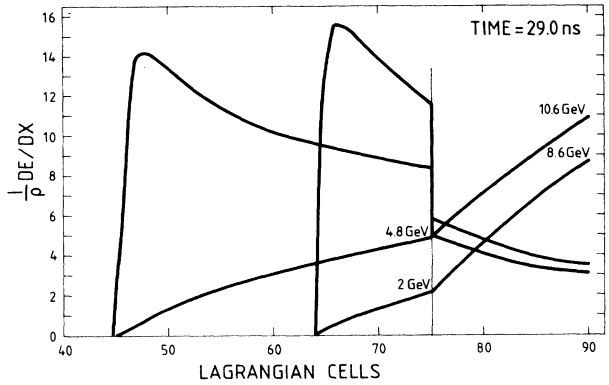

FIG. 16. Energy deposition and ion energy in HIBALL-I target with and without ion-energy increase, showing range shortening at 29.0 ns.

where

$$E(t)=\begin{cases}E_0, & t<t_1 \\ E_0+\Delta E, & t>t_2\end{cases} \tag{33}$$

$$dR/dt=(dR/dE)(dE/dt)=A\alpha E^{\alpha-1}\frac{\Delta E}{(t_2-t_1)}E_0 \tag{35}$$

$$=\alpha R(E)\frac{\Delta E}{(t_2-t_1)}\frac{1}{E(t)}\ . \tag{36}$$

If $\alpha=1.5$, $R(E)=0.2$ g/cm^2, $\Delta E=2.0$ GeV, $t_2-t_1=7$ ns, $\rho=1$ g/cm^3, and $E(t)=10$ GeV, then $\rho^{-1}\,dR/dt=8\times10^6$ cm/s.

At 2.5×10^6 K and 7 ns in Li-Pb, the Marshak wave will travel at 5.6×10^6 cm/s. This is seen to be slower than the ion ablation wave. The speed of the latter can be increased by increasing ΔE, say to 4 GeV, which doubles the speed to 1.6×10^7 cm/s, which is much faster than the Marshak wave. The speed of the Marshak wave is much slower in lead, being reduced by roughly a factor of 30, due to the much smaller mean free path. Opacities are taken from Refs. 149—151,195 with division by 3 to allow for bound-bound transitions[196] in high-atomic-number materials. At 29.9 ns the energy deposition (Fig. 16) and implosion in both cases are shown, for the HIBALL-type target with and without ion-energy ramping, Figs. 17 and 18. In the case without ramping the range is coming back to the lead—lead-lithium boundary. With ramping the energy has had to be increased to 10.9 GeV in order to compensate for the range shortening. Radiation conduction also contributes to this process with one or the other dominating depending on which moves the ablation front forwards most quickly.

The pellet gain with a fixed range was found to be 179.[11,12,14] When realistic energy deposition is included the gain falls to zero because the mass of the compressed part of the pusher which, together with the fuel, forms the payload is too large for it to be accelerated to the requisite velocity required for ignition. This confirms preliminary results given in Ref. 14. With ion-energy ramping the gain can be restored to 165. Inclusion of nonlocal α-particle transport[164] plus a corrected DT cross section brings the gain down to 150. A full set of results with ramping are included in Tables II and III. The above calculations did not include radiation conduction but all further calculations do include radiation conduction in the compression phase although in some of them it does not play an important role. In the burn phase we only consider Bremsstrahlung radiation losses, which is a reasonable approximation for the ignition. The effect of radiation transport on the ignition and burn of inertial fusion tar-

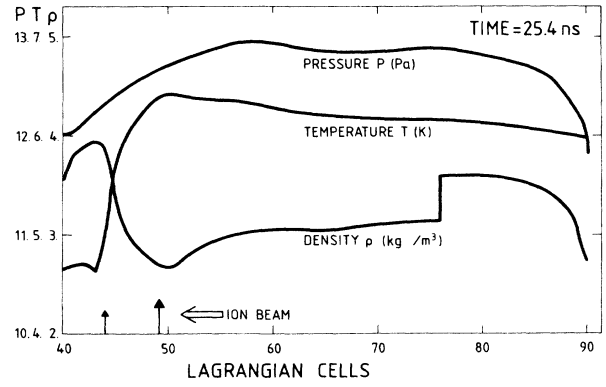

FIG. 15. Implosion of a HIBALL-I target with ion-energy increase at 25.4 ns. The ordinate scale is $\log_{10}$.

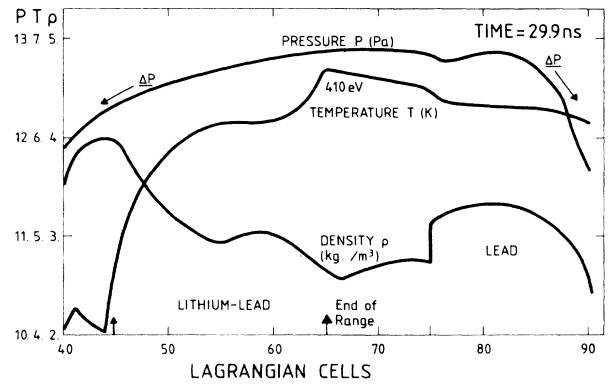

FIG. 17. Implosion of a HIBALL-I target at 29.9 ns without ion-energy ramping. The ordinate scale is $\log_{10}$.

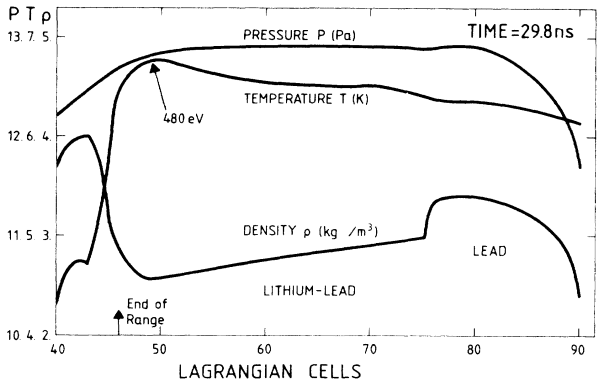

FIG. 18. Implosion of a HIBALL-I target at 29.8 ns with ion-energy increase. Results are given in Table II. All scales are $\log_{10}$ on the ordinate.

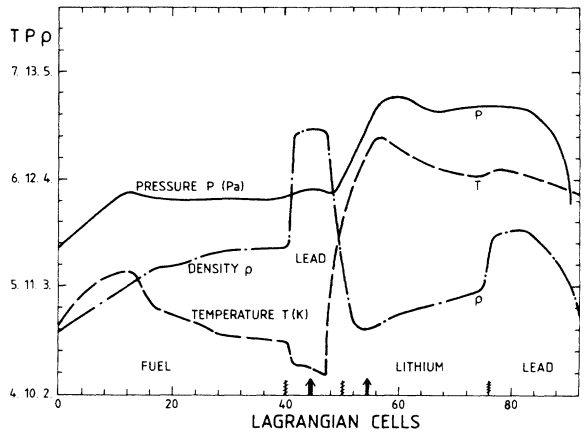

FIG. 19. Implosion of a HIBALL-II target (6-μm lead shield) at 25.2 ns. Results and parameters are given in Table III. Ordinate scale is $\log_{10}$.

gets has been reported upon in Refs. 7, 85, 90, and 176.

In Fig. 19 we show an implosion of a HIBALL-II -type pellet with a 5-μm-thick lead layer and a 600-μm-thick lithium layer at 25.2 ns, using 550 TW for the main pulse. The range shortening is compensated for by raising the ion energy from 8.0 to 10.3 GeV over a period of 21—27 ns. Radiation conduction is included in the calculation but does not play an important role because the ablation front is moved faster by the ions. The maximum temperature is 215 eV, so that any Marshak wave would move rather slowly. The pellet ignites and yields a gain of 149. The full set of results is given in Table III. The deposition profiles as 23.06 and 29.9 ns are shown in Figs. 20 and 21. In Fig. 22 we show the implosion of a HIBALL-II-type target with a 30-μm-thick lead layer. We employ the technique introduced by Hazlet *et al.* and ramp the ion energy so strongly that the ions enter into the lead and ablate part of this away. It is claimed[18] that this yields a better compression. The ion energy is ramped from 8.0 to 11.6 GeV over a time from 23 to 28 ns. Here also the temperature at 28.5 ns is only 240 eV so radiation effects (although included) do not play any decisive role. For this target the ignition configuration is shown in Fig. 23. Ignition occurs at 42.75 ns, much later than 36.6 ns registered for the HIBALL-I target because the payload is much more massive. The gain achieved is 166. A full set of results are given in Table V.

In the next calculation we tried to implode a HIBALL-I-type target using radiation transport alone to compensate for the range shortening. The range shortening is, however, quite large, as the deposition goes back towards the lead tamper. Therefore in order to make the radiation wave travel fast enough we had to raise the temperature by raising the power to 750 TW. However, unfortunately this causes increased range shortening due to the temperature rise and the transfer of bound to free electrons. We show a successful implosion at 25.4 ns in Fig. 24 where one can see a Marshak wave with a temperature of 200 eV compensating for the range shortening. The rest of the

TABLE I. Comparison of experimental results and calculated results for the energy deposition of uranium ions of different energy in room-temperature gold.

E (GeV)	$\rho^{-1}dE/dx$ (keV cm^2/g) Expt.	Calc.
2.5	5×10^7	5.14×10^7
1.25	4.6×10^7	4.82×10^7
0.62	4.1×10^7	4.15×10^7
0.3	3.1×10^7	3.01×10^7

TABLE II. HIBALL-I target with range shortening and compensation by ion-energy ramping.

Input parameter	Units	Results
Prepulse power P_1	(TW)	2.4
Intermediate pulse power P_2	(TW)	30.1
Main pulse power P_3	(TW)	630
Prepulse duration τ_1	(ns)	15
Middle pulse duration τ_2	(ns)	6
Linear rise time τ_3	(ns)	3
Main pulse time τ_4	(ns)	7
Input energy	(MJ)	4.98
Initial energy of Bi^+ ions	(GeV)	8.6
Final energy of Bi^+ ions	(GeV)	10.8
Initial time at which ion energy rises	(ns)	21.0
Time at which ion-energy rise ends	(ns)	28.0
Initial energy of ions entering lithium	(GeV)	2.93
Final energy of ions entering lithium	(GeV)	4.88
Thickness of tamper	(μm)	140
Thickness of lithium layer	(μm)	370
Thickness of radiation shield	(μm)	
Thickness of fuel layer	(μm)	150
Mass of fuel	(mg)	4.0
Gain		159.(7)
Output of energy	(MJ)	796.(7)

TABLE III. HIBALL-II target with range shortening and compensation by ion-energy ramping (6-μm lead shield).

Input parameter	Units	Results
Prepulse power P_1	(TW)	2.4
Intermediate pulse power P_2	(TW)	30.1
Main pulse power P_3	(TW)	630
Prepulse duration τ_1	(ns)	15
Middle pulse duration τ_2	(ns)	6
Linear rise time τ_3	(ns)	3
Main pulse time τ_4	(ns)	7
Input energy	(MJ)	4.99
Initial energy of Bi^+ ions	(GeV)	8.0
Final energy of Bi^+ ions	(GeV)	10.3
Initial time at which ion energy rises	(ns)	21.0
Time at which ion-energy rise ends	(ns)	28.0
Initial energy of ions entering lithium	(GeV)	2.18
Final energy of ions entering lithium	(GeV)	4.11
Thickness of tamper	(μm)	140
Thickness of lithium layer	(μm)	600
Thickness of radiation shield	(μm)	6
Thickness of fuel layer	(μm)	150
Mass of fuel	(mg)	4.0
Gain		149.(2)
Output of energy	(MJ)	746

pusher has been heated to 100 eV before the range has come back to its present position. By 29.9 ns the temperature, Fig. 25, has risen to 350 eV and the Marshak wave progresses far enough to produce a successful ignition at 39.7 ns. One needs 750 TW and 6.4 MJ to do this. The gain is 120. The results are described in detail in Table V. In general it proved harder to compensate for range shortening by radiation conduction than by voltage ramping. The temperatures needed are higher so the implosion is less efficient.

In Fig. 26 we show the implosion of a HIBALL-II target with a 6-μm lead layer. The range shortening is compensated for by radiation conduction only. We illustrate this by showing the temperature and density profiles at 29.08 and 39.5 ns. Ignition is reached at 41.87 ns. We used a power of 750 TW in the main pulse and 6.4 MJ. A full table of results is given in Table VI. The gain is 121.5. We show the ignition profile of the temperature in Fig. 27. The energy deposition profile at 29.08 ns is given in Fig. 28. This shows that the deposition has practically come back to the inner lead boundary of the tamper. Also in Table VI we show the results for a target in which the cavity-lithium-thickness region has been increased from 600—1000 μm. This allows more energy to be deposited in the lithium region even at high temperatures, as the ion energy can be increased to 90 GeV. This improved design was tuned to give a gain of 140. This maximized gain was achieved by doing calculations for various ion energies.

In conclusion we can say that both the HIBALL-I and HIBALL-II targets are viable targets. The HIBALL-I target is more stable in the pusher-fuel region. Due to ab-

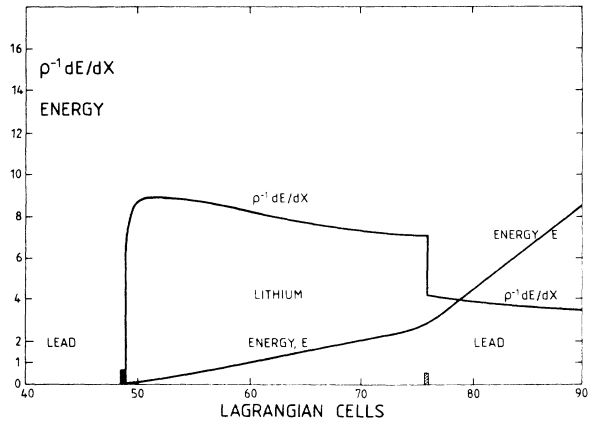

FIG. 20. Energy deposition in HIBALL-II target and ion energy at 23.06 ns with ion-energy ramping. Energy is in GeV.

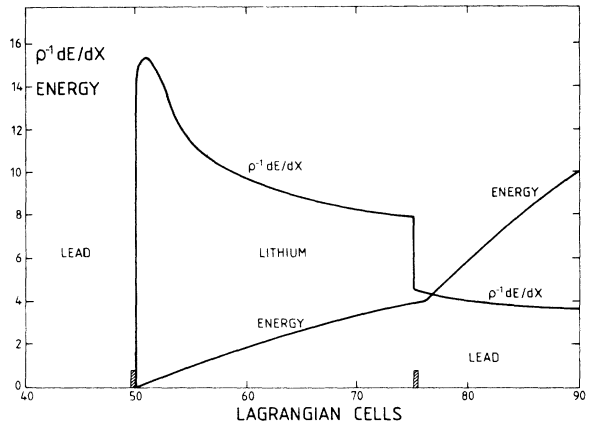

FIG. 21. Same as for Fig. 20 at 29.9 ns.

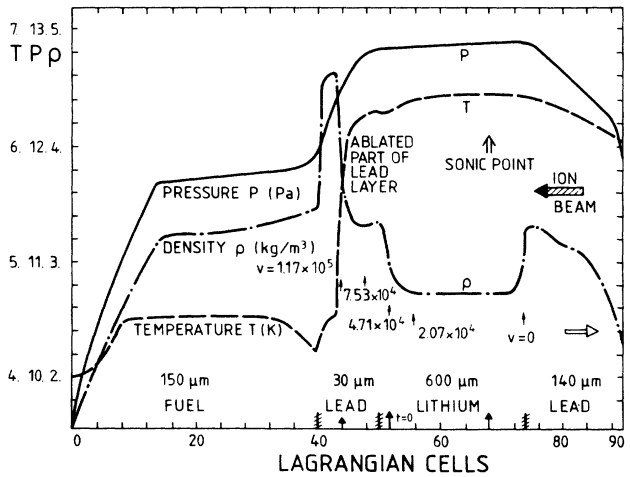

FIG. 22. Implosion of a HIBALL-II target with 30-μm lead shield at 28.5 ns and ion-energy ramping into lead shield. Results and parameters are given in Table IV. Velocity is in m/s.

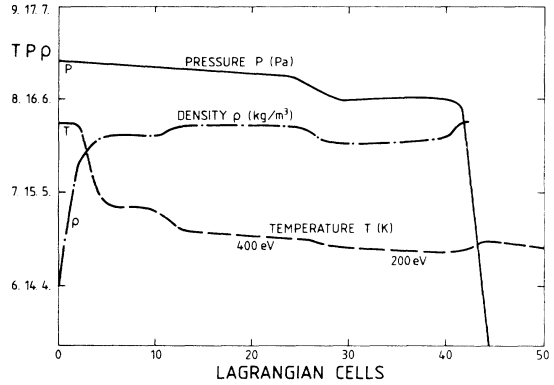

FIG. 23. Ignition profiles for HIBALL-II target at 42.75 ns. Details are given in Table IV. Ignition temperature is 5 keV.

lation the targets implode in a stable fashion. We discuss this later. It is easier to produce implosions by voltage ramping because one has some external control over the implosion. However, radiation can also be used to compensate for range shortening but one needs higher temperatures.

We now discuss two more calculations whose results are given in Tables VII and VIII. In Table VII we show details of a HIBALL-I calculation which includes realistic energy deposition, ion-energy ramping, and radiation transport (cf. calculation in Table II). In this case we were able to implode the target with 500 TW and an input energy of 4.42 MJ compared to 630 TW and 4.98 MJ. The ion energy needed to be increased slightly less, but the inclusion or of radiation conduction did not reduce this very much. It is not clear if the use of a lower power is due to the inclusion of radiation or due to better tuning of the pellet. The gain is reduced so clearly the compression obtained is less due to the lower power. Some of the other parameters are also different, for instance, the ramping takes place from 25 to 28 ns instead of from 21 to 28 ns in the first case. In Table VIII we present results from a HIBALL-II-type target with lead-lithium as pusher instead of lithium. The main pulse has a 650-TW power level, and the calculation includes ion-energy ramping from 8.6 to 10.9 GeV over a period 21–28 ns and includes radiation conduction. The lead shield has thickness of 10 μm. The input energy is 4.98 MJ and this target gives the highest gain of 171. This shows that a high compression was achieved in this calculation.

TABLE IV. HIBALL-II target with range shortening and compensation by ion-energy ramping and radiation transport and 30-μm-thick lead shield.

Input parameter	Units	Results
Prepulse power P_1	(TW)	11.3
Intermediate pulse power P_2	(TW)	24.0
Main pulse power P_3	(TW)	630
Prepulse duration τ_1	(ns)	15
Middle pulse duration τ_2	(ns)	6
Linear rise time τ_3	(ns)	3
Main pulse time τ_4	(ns)	7
Input energy	(MJ)	5.13
Initial energy of Bi^+ ions	(GeV)	8.0
Final energy of Bi^+ ions	(GeV)	11.6
Initial time at which ion energy rises	(ns)	23.0
Time at which ion-energy rise ends	(ns)	28.0
Initial energy of ions entering lithium	(GeV)	2.18
Final energy of ions entering lithium	(GeV)	5.91
Energy of ions entering lead shield	(GeV)	2.32
Thickness of tamper	(μm)	140
Thickness of lithium layer	(μm)	600
Thickness of pusher lead shield	(μm)	30
Thickness of fuel layer	(μm)	150
Mass of fuel	(mg)	4.0
Gain		165.(6)
Output of energy	(MJ)	849.(5)

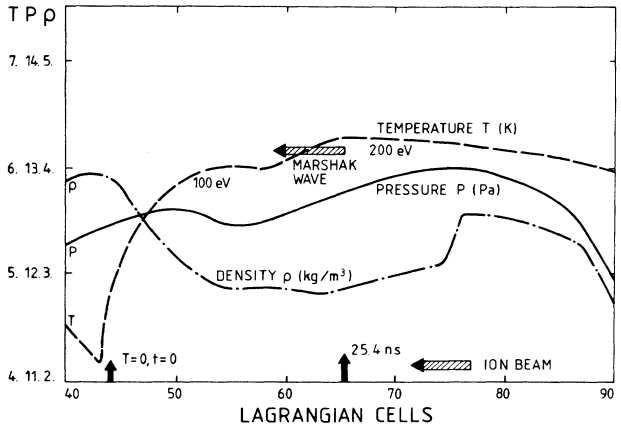

FIG. 24. Implosion of a HIBALL-I target with range shortening compensated by radiation at 25.4 ns. See Table V for results.

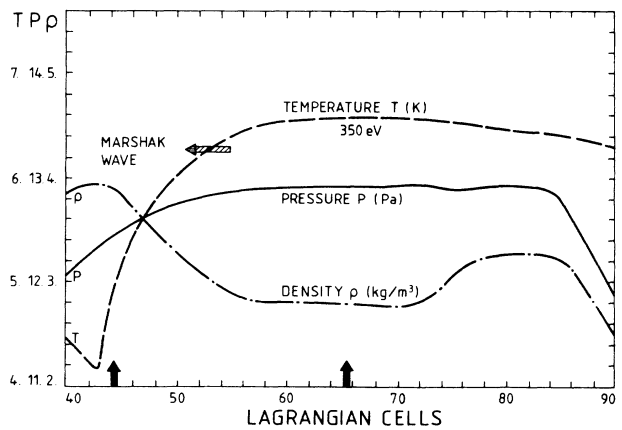

FIG. 25. Implosion of a HIBALL-I target with range shortening compensated by radiation transport at 29.9 ns. Results and parameters are given in Table V.

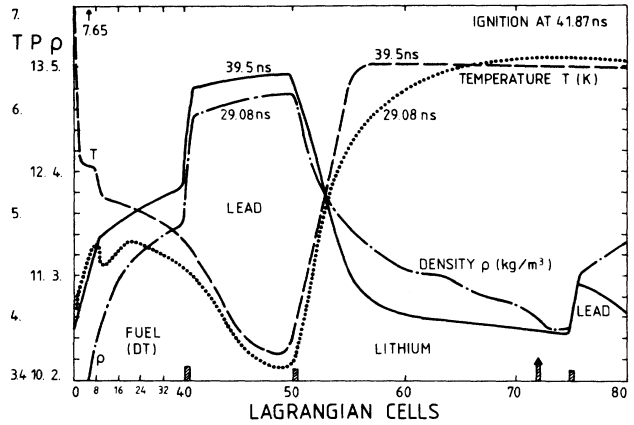

FIG. 26. Implosion of a HIBALL-II target with radiation compensation for range shortening at 29.08 and 39.0 ns. Ignition is at 41.87 ns. Details of results and parameters are given in Table VI. The ignition temperature is 8.5 keV.

We note that the HIBALL-II-type-target design implies the inclusion of a radiation shield as its basic element. However, various improvements and variations on this basic theme have been calculated. The basic HIBALL-II-type target is unstable at the boundary between the radiation shield and the fuel. This can cause mixing of lead into the fuel after the void closes and the fuel and the radiation shield decelerate. This situation can be ameliorated by the inclusion of low-ρ, low-Z material(s) such as lithium between radiation shield and the fuel (one can, of course, also include more DT, but this could be more expensive). This design has been calculated in Refs. 7 and 43 and 85, 86, and 87.

TABLE V. HIBALL-I with radiation compensation and no ramping of ion-energy.

Input parameter	Units	Results
Prepulse power P_1	(TW)	2.4
Intermediate pulse power P_2	(TW)	30.1
Main pulse power P_3	(TW)	750
Prepulse duration τ_1	(ns)	15
Middle pulse duration τ_2	(ns)	6
Linear rise time τ_3	(ns)	3
Main pulse time τ_4	(ns)	7
Input energy	(MJ)	6.57
Initial energy of Bi^+ ions	(GeV)	8.6
Final energy of Bi^+ ions	(GeV)	8.6
Time at which ion energy rises	(ns)	
End time of ion-energy rise	(ns)	
Initial energy of ions entering lithium	(GeV)	2.93
Final energy of ions entering lithium (main pulse)	(GeV)	2.04
Thickness of tamper (lead)	(μm)	140
Thickness of lithium layer (lithium-lead)	(μm)	370
Thickness of radiation shield	(μm)	
Thickness of fuel layer	(μm)	150
Gain		118.9
Output of energy	(MJ)	781

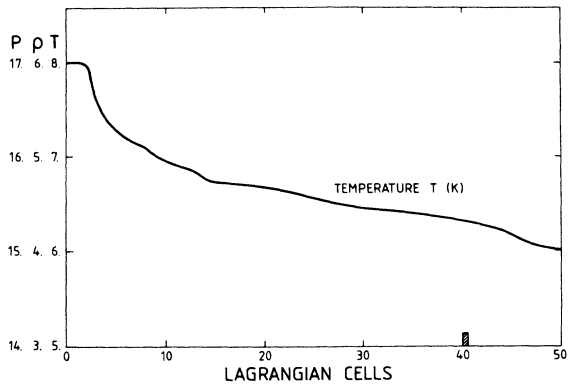

FIG. 27. Temperature ignition profile at 41.87 ns for target of Fig. 26.

IV. THE STABILITY OF INERTIAL-CONFINEMENT-FUSION PELLET IMPLOSIONS

A. Density gradient and ablation-induced stabilization of the Rayleigh-Taylor instability in inertial-confinement-fusion pellet implosions

One of the most critical problems for inertial fusion is the occurrence and possible suppression of the Rayleigh-Taylor instability, at least to the extent that the shell does not break and one obtains ignition and propagating burn and a sufficiently high gain. This instability occurs when the low-density hot plasma is pushing the cold much-denser pusher part of the payload. Across this region the pressure is decreasing inwards (Fig. 17), and the density is increasing inwards so that $\nabla P \times \nabla \rho$ is negative. It also occurs after void closure when the denser fuel is decelerating the pusher. In the first case the instability is due to the formation of bubbles and spikes, and it can cause the shell to break up with consequent pusher-fuel mixing, which causes loss of compression which leads to a loss of gain or even a failure to ignite. The second case also leads to very bad pusher-fuel mixing, which, when the pusher is a high-Z material, causes poor burn conditions due to an increase in Bremsstrahlung radiation.

In the case of ion-beam-driven inertial fusion, the stability question[6,7,11] has been analyzed by Lindl

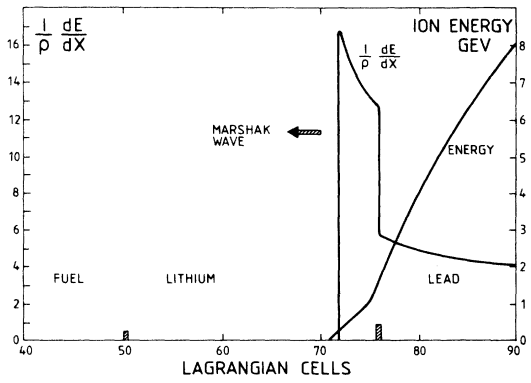

FIG. 28. Energy deposition for target in Fig. 26 at 29.9 ns.

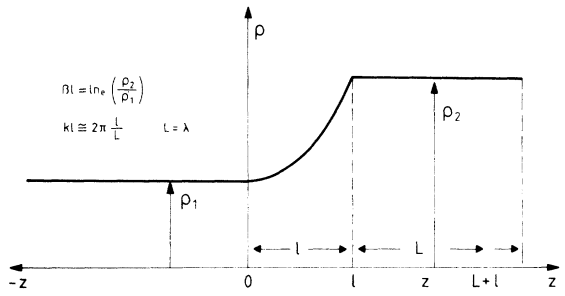

FIG. 29. Density profile and definition of variables for an implosion with a density gradient to be used in the Rayleigh analysis of the Rayleigh-Taylor instability with a density gradient.

et al.,[197,198] McCrory *et al.*[199], Long and Tahir[6,7] and Metzler and Meyer-ter-Vehn[78] among others. In the first three cases the stabilization due to a density gradient has been investigated for the case of laser driven and ion-beam-driven implosions. Recently, Mikaelian[198,200–202] has developed solutions for any step-like density profile. However, here we restrict ourselves to the use of an exponential density gradient in our analysis because there is an exact analytic solution derived by Raleigh.[203,204] Bodner[205] and Takabe *et al.*[206,207] have investigated the Rayleigh-Taylor instability in an ablating plasma, and we also investigate this problem specifically for the case of ion-beam-driven implosions.

TABLE VI. HIBALL-II target with radiation compensation for range shortening and no ion-energy ramping.

Input parameter	Units	Results I	Results II
Prepulse power P_1	(TW)	2.4	2.4
Intermediate pulse power P_2	(TW)	30.1	30.1
Main pulse power P_3	(TW)	750	750
Prepulse duration τ_1	(ns)	15	15
Middle pulse duration τ_2	(ns)	6	6
Linear rise time τ_3	(ns)	3	3
Main pulse time τ_4	(ns)	7	7
Input energy	(MJ)	6.58	6.58
Initial energy of Bi^+ ions	(GeV)	8.0	9.0
Final energy of Bi^+ ions	(GeV)	8.0	9.0
Initial time at which ion energy rises	(ns)		
Time at which ion-energy rise stops	(ns)		
Initial energy of ions entering lithium	(GeV)	2.18	3.42
Final energy of ions entering lithium	(GeV)	0.94	2.44
Thickness of tamper	(μm)	140	140
Thickness of lithium layer	(μm)	600	1000
Thickness of radiation shield	(μm)	6	6
Thickness of fuel layer	(μm)	150	150
Mass of fuel	(mg)	4.0	4.0
Gain		121.5	140
Output of energy	(MJ)	800.	933

TABLE VII. HIBALL-I target with range shortening and compensation by ion-energy ramping and radiation transport.

Input parameter	Units	Results
Prepulse power P_1	(TW)	2.4
Intermediate pulse power P_2	(TW)	30
Main pulse power P_3	(TW)	500
Prepulse duration τ_1	(TW)	15
Middle pulse duration τ_2	(ns)	6
Linear rise time τ_3	(ns)	3
Main pulse time τ_4	(ns)	7
Input energy	(MJ)	4.42
Initial energy of Bi^+ ions	(GeV)	8.6
Final energy of Bi^+ ions	(GeV)	10.5
Initial time at which ion energy rises	(ns)	25.0
Time at which ion-energy rise ends	(ns)	28.0
Initial energy of ions entering lithium-lead	(GeV)	2.93
Final energy of ions entering lithium-lead	(GeV)	4.60
Thickness of tamper	(μm)	140
Thickness of lithium-lead layer	(μm)	370
Thickness of lead radiation/ pusher shield	(μm)	
Thickness of fuel layer	(μm)	150
Mass of fuel	(mg)	4.0
Gain		134
Output of energy	(MJ)	592

TABLE VIII. HIBALL-II target (DT-Pb-Pb—Li-Pb) with realistic energy deposition plus compensation for range shortening by ion-energy ramping and radiation transport.

Input parameter	Units	Results
Prepulse power P_1	(TW)	2.4
Intermediate pulse power P_2	(TW)	30.0
Main pulse power P_3	(TW)	650.0
Prepulse duration τ_1	(ns)	15.0
Middle pulse duration τ_2	(ns)	6.0
Linear rise time τ_3	(ns)	3.0
Main pulse duration τ_4	(ns)	7.0
Initial energy of Bi^+ ions	(GeV)	8.6
Final energy of Bi^+ ions	(GeV)	10.9
Initial time at which ion energy rises	(ns)	21.0
Time at which ion-energy rise ends	(ns)	28.0
Initial energy of ions entering lithium-lead	(GeV)	2.93
Final energy of ions entering lithium-lead	(GeV)	5.42
Thickness of tamper	(μm)	140
Thickness of lithium-lead layer	(μm)	370
Thickness of lead radiation shield	(μm)	10
Thickness of fuel layer	(μm)	150
Input energy	(MJ)	4.98
Output energy	(MJ)	856
Gain		171(7)

Lindl *et al.*[202] suggested the use of a density gradient as a stabilization mechanism. The density gradient must be produced in such a way that the mass of the payload is not increased, otherwise the hydrodynamic efficiency of the implosion decreases, with consequent loss of ignition. A density gradient can be achieved by a spread of ion energies within the ion beam, but it is also naturally produced by range shortening and eventual compensation by radiation or voltage ramping which increases the ion energy during the implosion. The stability of this whole process needs to be investigated because it requires exact spherical compensation over large distances.

The Rayleigh-Taylor instability with an exponential density gradient was solved exactly by Rayleigh,[203] and the solution has been discussed by Chandrasekhar[208] and recently by Mikaelian,[198,200–202] Kull,[209] and Jacobs.[210] Rayleigh discussed the two important types of behavior, namely, when βl is large and one obtains the discontinuity solution for the growth rate γ,

$$\gamma=(gkA)^{1/2}\ , \tag{37}$$

where g is the acceleration, $k=2\pi/\lambda$, λ is the wavelength, and A is the Attwood number, $A=(\rho_2-\rho_1)/(\rho_2+\rho_1)$, and the case where βl (Fig. 29) is small. Here we have used a calculator to obtain a numerical solution. Different algorithms are used in different regions of the parameter space in order to obtain convergence of the nonlinear equations. In the following we discuss these solutions and their application to ion-beam-fuison implosions.

The solution is given by two equations in Ref. 203, namely, Eqs. (31) and (32) (see Fig. 29 for definitions of β and l), which are reproduced here as Eqs. (38) and (40),

$$\frac{4kl\theta}{(\beta^2l^2-4k^2l^2-\theta^2)}=\tanh\left[\frac{\theta}{2}\right] \tag{38}$$

or

$$\theta\coth\left[\frac{\theta}{2}\right]=\left[\frac{(\beta l)^2-4(kl)^2}{4kl}\right]-\frac{\theta^2}{4kl} \tag{39}$$

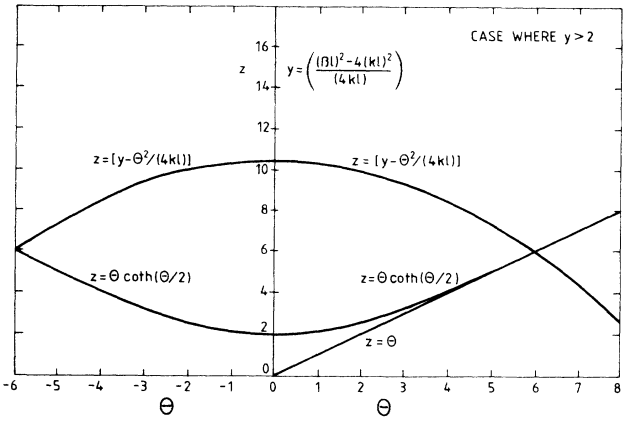

FIG. 30. Solution of Rayleigh problem for $y>2$ (see text for details, Sec. IV A).

and

$$n^2=\frac{-4(kl)^2g\beta}{[(\beta l)^2+4(kl)^2-\theta^2]} \tag{40}$$

$$=\frac{-4(kg)kl\beta l}{[(\beta l)^2+4(kl)^2-\theta^2]}\ . \tag{41}$$

Equation (38) or (39) has to be solved for θ, which when substituted in Eq. (40) or (41) gives n^2, the growth rate squared. The density profile is shown in Fig. 29. The density for all values of $z<0$ is ρ_1 and for all values greater than l is $\rho_2=\rho_1\exp(\beta l)$. The transition from one density to the other is $\rho_2=\rho_1\exp(\beta z)$.

There are many solutions to these equations but one is interested in the solution with the greatest growth rate. When the parameter $y=[(\beta l)^2-4(kl)^2]/4kl$ is greater then 2, θ is real, and when $y<0$, $\theta=i\phi$ is imaginary. When $y=2$, $\theta=\phi=0$. The largest growth rate is obtained by the largest value of θ and the smallest value of ϕ. When $y<0$,

$$n^2=\frac{-4gk\beta lkl}{[(\beta l)^2+4(kl)^2+\phi^2]}\ , \tag{42}$$

$$n^2=\begin{cases}\dfrac{-kg\beta l}{[2kl+\phi\cot(\phi/2)]}, & y<0 \qquad (43)\\[2ex] \dfrac{kg\beta l}{[2kl+\theta\coth(\theta/2)]}, & y>0\ . \qquad (44)\end{cases}$$

One can see that $\phi=\phi(kl,\beta l)$, or $\theta=\theta(kl,\beta l)$ and that

$$n^2=-kgn'(\beta l,kl,\phi) \tag{45}$$

$$=-kgn'(\beta l,kl)\ . \tag{46}$$

For the determination of θ or ϕ, y and kl serve as useful independent parameters.

In order to apply the theory to the analysis of pellet calculations a number of approximations need to be made. The theory needs to be applied to a shell of thickness L which is being accelerated either by ablation or by a pressure from a hot expanding gas. We assume that the wavelength with the greatest growth rate is that which is equal to L. The parameter β can be determined from the simulations as the inverse of the length over which the density is falling. One needs to evaluate the parameters βl and kl,

$$\beta l=\ln(\rho_2/\rho_1),\quad kl=kL(1/L)\cong 2\pi l/L\ . \tag{47}$$

l is determined from the simulations, as are ρ_2/ρ_1 and L.

From the parameters βl, kl, and $k=2\pi/L$, the fastest growth rate can be determined (and by working out the growth rate as a function of k, the most dangerous wavelength can also be evaluated). It is useful to work out analytically two limiting cases. When $[(\beta l)^2-4(kl)^2]/4kl$ becomes very large the solution for θ is βl, as can be seen from Fig. 30. Around this point one can use $\theta=\beta l$ as the starting point for an iterative solution. One has

$$\left[\frac{(\beta l)^2-4(kl)^2}{4kl}\right]-\theta\coth(\theta/2)=\theta^2/(4kl) \tag{48}$$

and by substituting $\theta=\beta l$ into the expression $\theta\coth(\theta/2)$,

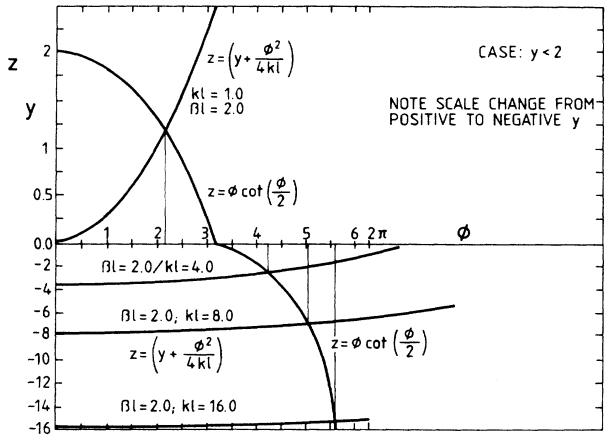

FIG. 31. Same as in Fig. 30 for $y<2$.

$$\theta^2=(\beta l)^2-4(kl)^2-4kl\beta l\coth(\beta l/2)\ , \tag{49}$$

$$n^2/gk=\frac{-[4(kl)(\beta l)]}{[8(kl)^2+4(kl)(\beta l)\coth(\beta l/2)]} \tag{50}$$

$$=\frac{-\beta l}{[2kl+(\beta l)\coth(\beta l/2)]}\ . \tag{51}$$

For $kl\ll\beta l$, one obtains the result

$$n^2/gk=-\tanh(\beta l/2)=-gkA\ , \tag{52}$$

$$A=(\rho_2-\rho_1)/(\rho_2+\rho_1)=\tanh(\beta l/2)\ . \tag{53}$$

This is the standard result for a large density jump.

When $[(\beta l)^2]-4(kl)^2]/4kl$ is large and negative, $kl\gg\beta l$. In this case $\theta=i\phi$,

$$\frac{n^2}{gk}=\frac{-4kl\beta l}{[(\beta l)^2+4(kl)^2+\phi^2]}\ , \tag{54}$$

and one looks for the solution with the smallest ϕ,

$$\phi\cot(\phi/2)=\frac{(\beta l)^2-4(kl)^2}{4kl}+\frac{\phi^2}{4kl}\ . \tag{55}$$

Since $kl>\beta l$, $\phi\sim 2\pi$, then (see Fig. 31)

$$\cot(\phi/2)=-kl/\phi\ . \tag{56}$$

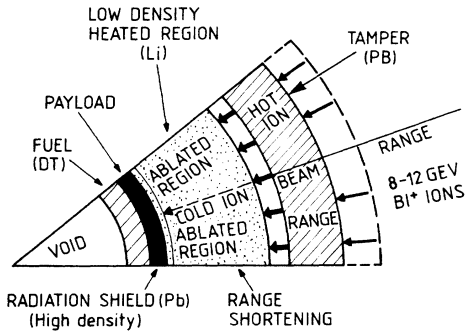

FIG. 32. Target in its working configuration with range shortening and ablation, plus compensation by radiation transport or ion-energy ramping.

Since

$$n^2/gk=\frac{-\beta l}{2kl+\phi\cot(\phi/2)} \tag{57}$$

$$\cong-[\beta l/kl]\ , \tag{58}$$

$$n^2\cong-g\beta\ . \tag{59}$$

When kl is small and $\beta l\ll kl$, $y=0$,

$$\phi\cot(\phi/2)=\phi^2/4kl\ , \tag{60}$$

$$\phi^2=8kl\ . \tag{61}$$

Then, from

$$n^2/gk=\frac{-4kl\beta l}{[(\beta l)^2+4(kl)^2+8kl]} \tag{62}$$

$$\cong\frac{-4kl\beta l}{8kl}\cong\frac{\beta l}{2}\ , \tag{63}$$

$$n^2/gk=A,\ \text{where } A=\tanh\left[\frac{\beta l}{2}\right]\to\frac{\beta l}{2} \tag{64}$$

for $\beta l\to 0$. These limits are given by Rayleigh, but this represents a clearer and simpler analysis. The last case can be seen in another way from Fig. 31. When βl and kl are small and $\beta l\ll kl$, $y\to kl\sim 0$. The factor $\phi^2/4kl$ rises very quickly and so the solution is $\phi\sim 0$, or $\phi^2=8kl$. It should be noted that the solution $\theta=\phi=0$ is obtained when $y=2$. In this case,

$$n^2=\frac{-4kl\beta l}{[(\beta l)^2+4(kl)^2]} \tag{65}$$

and

$$(\beta l)^2-4(kl)^2=8kl,\ \ y=0\ , \tag{66}$$

$$n^2/gk=\frac{-\beta l}{(2kl+2)}=[2kl+(kl)^2]^{1/2}/(kl+1)\ . \tag{67}$$

The above solution Eq. (67) is valid near $\phi=\theta=0$. When $\cot(\phi/2)=0$, $\phi=\pi$,

$$n^2/gk=\frac{\beta l}{2kl}\ . \tag{68}$$

For this case,

$$\pi^2/4kl=\frac{4(kl)^2-(\beta l)^2}{4kl}\ , \tag{69}$$

$$n^2/gk=\frac{-4kl\beta l}{8(kl)^2-\pi^2}\ , \tag{70}$$

from formula (70),

$$n^2\cong\frac{-\beta l}{2kl-\pi^2/4kl}\ . \tag{71}$$

In Table IX we show the evaluation of n^2/gk when $y<0$, and compare the results to the approximate solution given by Rayleigh. One solves iteratively Eq. (55) for ϕ and then substitutes this result in Eq. (54). In Table X we show the results of some evaluation for $y>0$.

The above analysis has been used to analyze the stability of the implosion with and without ramping of the ion energy. In the first case one gets ignition and in the

TABLE IX. Evaluation of n^2/gk when $y<0$ and comparison with solutions given by Rayleigh.

βl	kl	n^2/gk	n^2/gk (Rayleigh)
1	0.01	0.444	
1	0.1	0.394	
1	0.2	0.386	
1	0.5	0.383	
1	1	0.38	0.385
1	2	0.28	0.294
1	4	0.20	$\beta l/kl$

second one does not, and so the second case may seem not to be relevant, but it is included to show what improvement one could obtain in the stability with a distributed deposition which very much favors the creation of a density gradient. Lindl[197] has suggested that this is one of the most promising ways to improve stability. In this analysis we have at first ignored ablation or the discontinuity in velocity between the pusher and the pushing material.

All calculations are carried out for the "most dangerous wavelength" here assumed to be $\lambda=1/L$, where L is the pusher thickness. More accurate calculations of this wavelength can be calculated within this model by evaluating the growth rate as a function of k for fixed l and βl.

We now discuss the stability results for the simulations made. We have from Eq. (54)

$$n^2/gk=\delta\ , \tag{72}$$

$$\delta=\frac{-4kl\beta l}{[(\beta l)^2+4(kl)^2+\phi^2]}\ . \tag{73}$$

We define $k'=\delta k$. Now $n=i\gamma$ and the growth rate is $\Gamma=\gamma t$, where the magnitude of growth is equal to exp $|\Gamma|$. In Table XI, we will compare the values of Γ at 26 ns for the HIBALL case,[11–14] the case with ramping, and the case without (Cases 1,2,3). These values are calculated using Eqs. (54) and (55) and solving Eq. (55) by iteration. Different iteration schemes have been used in different regions of parameter space. We use Γ as a figure of merit. Case 2 is much better than it seems because the acceleration is 50% higher than Case 1 because a higher power was used. Case 3 is much lower because the acceleration is much lower and δ is much smaller because of the fairly gradual density gradient. In Case 3 no ignition is achieved because the pusher velocity is too small (one is trying to accelerate too much mass with too little energy). One knows that γ depends essentially on the aspect ratio $(R_0/\Delta R_0)(R_0$ inner initial radius, ΔR_0 shell thickness) so in order to improve stability ΔR_0 must be larger. This requires a thicker pusher shell and hence higher input energy. The other factors which would improve stability are various suggested stabilizing mechanisms, one of which is ablation. If

TABLE X. Evaluation of n^2/gk when $y>0$.

βl	kl	n^2/gk
3.6	0	0.946
3.6	0.1	0.929
3.6	0.5	0.911
3.6	1.0	0.90

TABLE XI. Comparison of the values of Γ at 26 ns.

Case	Γ	δ
1	14.4	0.187
2	12.7	0.097
3	2.67	0.073

$$\Gamma=\gamma t=\sqrt{k'g}\,t=\sqrt{\delta kg}\ t\ \ (A=1) \tag{74}$$

(constant acceleration), and $g=2R_0/t_c^2$, where t_c is collapse time, then

$$\Gamma=\left[\delta\frac{2\pi}{\Delta R_0}\frac{2R_0}{t_c^2}\right]^{1/2}t_c=\left[4\delta\pi\frac{R_0}{\Delta R_0}\right]^{1/2}\ . \tag{75}$$

Therefore Γ is dependent on $\sqrt{\delta}$ and $\sqrt{(R_0/\Delta R_0)}$, where R_0 is the minimum in-flight pusher-shell thickness.

In target implosions the situation is very different from the classical case of two fluids of different density being accelerated. In this case the acceleration is considered to be imposed by an external force. In the case of ion-beam-driven target implosions, the acceleration is driven mainly by the thermal pressure generated in the fluid by the ion beam. A pressure gradient is developed between the end of the ion-beam range or the ablation-thermal front, where the Marshak wave has progressed to, and the inner front of the fuel. As the pressure is approximately constant across the thermal-ablation front, in the hot region the density is low and the temperature is high, whereas in the compressed part of the pusher, the density is high and the temperature is low (Fig. 32). The classical growth rate must be modified by the effects inherent at the pushing front, such as ablation-flow, radiation and electron conduction, a highly inhomogeneous density profile, the compressibility of the plasma, and the effects of a real equation of state. Also, however, the effect of realistic energy deposition should be taken into account together with range shortening and radiation or ion-energy-increase compensation. Here we discuss and apply a method which takes at least some of these effects into account. Because the effects taken into account were found to be inseparable it was found necessary for a quantitative study of the implosion stability to use a self-consistent treatment of the ablating plasma.[206,207]

In Refs. 206 and 207 the fluid equations are used in a frame moving with the ablation front which is accelerated by the ablation pressure. This effect is "simulated" by the introduction of an intertial force $\rho\mathbf{g}$ which is included in the equations of motion which are then given by,

$$\frac{\partial\rho}{\partial t}+\nabla\cdot\rho\mathbf{v}=0\ , \tag{76}$$

$$\rho\left[\frac{\partial}{\partial t}\mathbf{v}+\mathbf{v}\cdot\nabla\mathbf{v}\right]=-\nabla P+\rho\mathbf{g}\ , \tag{77}$$

$$\rho C_v \left[\frac{\partial T}{\partial t} + \mathbf{v}\cdot\nabla T \right] = -P\nabla\cdot\mathbf{v} + \nabla(K\nabla T) , \tag{78}$$

where ρ, $\mathbf{v}$, and T are the density, velocity, and temperature of the ablating plasma. An ideal-gas equation of state was used, together with a Spitzer electron conductivity K. However, even this approach has its limitations. Firstly, due to the double-layer effect,[211–213] the electron conductivity is very much reduced by a factor of ~ 20. Thus the real mechanism of conduction is radiation conduction in such inhomogeneous plasmas.[7,88,84,85] Then this approach does not include the realistic mechanism producing acceleration, namely, the energy deposition by ions. Further, one should also include the effects of a real equation of state. However, despite these limitations this approach represents a significant advance over previous treatments of the problem.

In Refs. 206 and 207 the background ablating plasma whose stability was investigated is the stationary solution to Eqs. (76)–(78). The solution in normalized form was found to be characterized by two dimensionless parameters (G,R_p), where $G=|g|/(c_s^2/R_s)$ where c_s is the velocity of sound at the sonic point and R_s is the radius of the sonic point. The sonic point is the point where the fluid velocity is the same as the local velocity of sound, and can be shown to be where the temperature profile has a maximum.[214–220] Further $R_\rho=\rho_a/\rho_s$, where ρ_a is the density at the ablation front (in the dense material) and ρ_s is the density at the sonic point. This ratio is of the order $10-10^2$ in our calculations.

The equations (76)–(78) are linearized in the deviation $f_1(\mathbf{r},t)$ from the zeroth-order solution $f_0(\mathbf{r})$. Separating variables with the aid of the expansion

$$f_1(\mathbf{r},t)=\sum_{l,m} f^{l,m}(r)\exp[\gamma(l)t]Y_m^l(\theta,\phi)$$

in spherical harmonics, where $\gamma(l)$ is the growth rate of mode l; the linearized equations are reduced to an eigenvalue problem for the $[f_1^{l,m}(r)$ with the growth rate $\gamma(l)$ as the eigenvalue.

Takabe *et al.*[206,207] found that the results for the growth rate could be fitted empirically by the simple analytic formulas

$$\gamma=\alpha\sqrt{kg}-\beta k v_a , \tag{79}$$

where $k=2\pi/\lambda=1/r_a$, where λ is the wavelength of the perturbation, r_a is the radius of the ablation front, and v_a is the ablation velocity (in the cold material). At the ablation front mass is conserved, so that

$$r_a^2\rho_a v_a = r_s^2\rho_s c_s , \tag{80}$$

$$v_a = r_s^2\rho_s c_s/(r_a^2\rho_a) , \tag{81}$$

where c_s is the velocity of sound at the sonic point, ρ_s is the density at the sonic point, ρ_a is the density of the ablating material, and r_s is the radius of the sonic point.

Takabe *et al.* found that

$$\alpha=0.9G^{-0.02} , \tag{82}$$

$$\beta=3.1G^{-0.2}(R_\rho/50)^{0.075} , \tag{83}$$

where $G=g/(c_s^2 r_s^{-1})$, g being the acceleration of the ablation front, and $R_\rho=(\rho_a/\rho_s)$.

From the expression for the growth rate γ one can see that above a certain wave number k_c perturbations do not grow and that there is a wave number k_m at which the growth rate is a maximum. One can find k_c by setting $\gamma=0$,

$$\alpha^2 k_c g=\beta^2 k_c^2 v_a^2 , \tag{84}$$

$$k_c=\alpha^2 g/\beta^2 v_a . \tag{85}$$

Since $g=P_a/(\rho_a\,\Delta R_a)$ where P_a is the ablation pressure and ΔR_a is the in-flight shell thickness, and

$$P_a=2\rho_s c_s^2 .$$

Then

$$k_c=2\alpha^2 r_a^4 R_\rho/(\beta^2 r_s^4\Delta R_a) . \tag{86}$$

One can find k_m by setting $d\gamma/dk=0$,

$$\tfrac{1}{2}\alpha\sqrt{(g/k_m)}=\beta v_a , \tag{87}$$

$$k_m=\tfrac{1}{4}\alpha^2 g/(\beta^2 v_a^2) , \tag{88}$$

$$l_m=k_m r_a=\tfrac{1}{4} r_a\alpha^2 g/(\beta^2 v_a^2) . \tag{89}$$

There is thus a natural wave number at which the growth rate is a maximum in this theory and this has been confirmed by analytic calculations,[216] which we discuss briefly below. Previously this wave number at which the growth rate is a maximum was taken to be $k_m=2\pi/\Delta R_{\min}$ where $\Delta R_{\min}$ is the minimum in-flight shell thickness. It was argued that small k values grew more slowly due to the formula for the growth rate, and larger k values for which $\lambda<\Delta R_{\min}$ grew more slowly due to nonlinear saturation effects.

The growth rate is $\exp(\gamma t_c)$, where t_c is the implosion time. Using the classical expression one obtained $\Gamma_m=\gamma_m t_c$ which gives

$$\Gamma_m^{\rm cl}=2\sqrt{\pi A} , \tag{90}$$

where $A=R_0/\Delta R_{\min}$, and R_0 is the initial shell radius. Using $g=P_a/\rho_a\Delta R_{\min}$ and $P_a=2\rho_s c_s^2=2v_a^2\rho_a^2 r_a^4/(\rho_s^2 r_a^4)$, we obtain

$$\Gamma_m^{\rm abl}=\gamma_m t_c=\tfrac{1}{2}(\alpha^2/\beta)\sqrt{A}\,(r_a/r_s)^2(\rho_a/\rho_s)^{1/2} . \tag{91}$$

If one assumes that $(r_a^2/r_s^2)(\rho_a/\rho_s)^{1/2}\cong 1$, then

$$\Gamma_m^{\rm abl}=\tfrac{1}{2}(\alpha^2/\beta)\sqrt{A} . \tag{92}$$

Therefore

$$\Gamma_m^{\rm abl}=\tfrac{1}{2}(\alpha^2/2\beta\sqrt{\pi})\Gamma_m^{\rm cl} . \tag{93}$$

For example, if $\alpha=1$, and $\beta=3$,

$$\Gamma_m^{\rm abl}=\Gamma_m^{\rm cl}/21 . \tag{94}$$

If we put $2\pi/\Delta R_{\min}=\bar{k}_m$, then for the pellet calculations reported on in this paper since $\Delta R_{\min}$ is small $k_m \ll \bar{k}_m$. Therefore $k_m g \ll \bar{k}_m g$. Further, the growth rate $\gamma(k_m)$ is half the classical value at k_m. However, the important point remains that the reduction in the growth rate occurs mainly because the high growth rates at high k values are

stabilized by ablation, so that the k value of maximum growth is substantially reduced. The further reduction of 50% over the classical value is an extra bonus, but it is not as significant.

In our calculations

$$c_s=\sqrt{P/\rho}=10^5 \text{ m/s} \tag{95}$$

and using $v_a=(r_s/r_a)^2(\rho_s/\rho_a)c_s$ for the ablation velocity and $(r_s/r_a)\sim 3$, $\rho_s/\rho_a\sim 10^{-2}$, we obtain $v_a\sim 10^4$ m/s. Therefore for $\alpha=1$, $\beta=1$, 2, 3, and 4, $\exp(\Gamma_m)$ is given by 50, 7, 4, and 3 where $g\sim 10^{13}$ m/s^2 and the time of the implosion is taken to be 10 ns. These growth rates are considerably smaller than those obtained without consideration of convective stabilization. A typical value of β in our calculations is 2. However, the results are very sensitive to the values of g and v_a. One can also estimate the value of v_a by calculating the velocity of the Marshak wave. This starts from the end of the hot range and travels 200 μm. This yields an average v_a of 3.10^4 m/s. Further, one can use

$$v_a=(\rho_a \bar{A})^{-1} dm/dt \ , \tag{96}$$

where dm/dt is the mass-ablation rate, $\bar{A}$ is the area, and ρ_a is the density. The mass ablated is 40 mg and $\rho_a=10^4$ kg/m^3. The area is 1.2×10^{-6} m^2, and $v_a=4\times 10^4$ m/s. These values give very low growth rates.

Finally, we note that Kull and Anisimov[216] have obtained similar results to Takabe *et al.* using analytic methods. In their work a generalized surface wave-dispersion relation for arbitrary step profiles is derived. This allows them to give a systematic overview of different regimes of convective stabilization and the connected growth reduction. Numerical solution of their analytic results for the growth rate give results similar to those of Takabe *et al.* Recent work by Emery, Gardner, and Bodner[217] also shows reductions of the growth rate for implosions driven by short wavelength lasers by factors of three to four. This is also said to be due to mass ablation. However, the calculations are in two dimensions and this allows the introduction of vorticity into the problem. The authors then state that it is the ablative convection of vorticity away from the unstable ablation surface which both controls the interchange of the two fluids and leads to the reduction of the growth rate. In respect to energy deposition an ion beam is, of course, like a fictitious laser beam of zero wavelength. Thus with an ion beam one would expect even greater reductions in the growth rate according to these calculations.

V. ANALYTIC THEORY OF THE IMPLOSION, IGNITION, AND BURN PHASES OF INERTIAL-CONFINEMENT-FUSION PELLET DYNAMICS

A. Theoretical analysis of pellet dynamics, including ablation, compression, ignition, burn, and gain

In order to reduce the input energy needed to compress and ignite a pellet it is important to have a high beam-fuel coupling efficiency.[14] This efficiency can be expressed as $\eta_{\rm DF}$,

$$\eta_{\rm DF}=\eta_{\rm abs}\eta_{\rm AP}\eta_{\rm PF} \ , \tag{97}$$

where $\eta_{\rm abs}$ is the absorption efficiency of ion-beam energy into thermal energy in the pellet and is ~ 1. $\eta_{\rm AP}$ is the efficiency with which energy is transformed from absorber energy into kinetic energy of the pusher shell, which moves inwards. Most of the ion-beam energy is used to heat the lead tamper and the lithium layer which produces the thermal and ablation pressure which drives the payload including the fuel inwards. This energy includes the energy needed to ionize the atoms. $\eta_{\rm PF}$ is the efficiency with which energy is transferred from the payload kinetic energy into energy for the fuel. Some energy is used to heat the fuel and some is for compression,

$$\eta_{\rm PF}=\frac{\frac{1}{2}m_F V_p^2}{\frac{1}{2}m_p V_p^2+\frac{1}{2}m_F V_p^2} \tag{98}$$

$$=\frac{m_F}{m_p+m_F} \ . \tag{99}$$

where V_p is the velocity of the payload needed to produce ignition $\sim 3\times 10^7$ cm/s, m_F is the mass of the fuel, and m_p is the mass of the payload comprising the fuel and the inward-moving part of the pusher shell composed of lead, lithium, or lead-lithium as the case may be, so denoted by $m_p^{\rm Pb/Li}$, where

$$m_p=m_p^{\rm Pb/Li}+m_F \tag{100}$$

The fuel mass is an input parameter for the model as is the initial inner radius of the fuel. The mass $m_p^{\rm Pb/Li}$ is determined by the condition that this layer should be thick enough to protect the fuel from radiation preheat, by the Marshak wave[6,7,43,81–97] or by high-energy photons, and that after ablation it is thick enough not to be broken through by the bubbles and spikes produced by the Rayleigh-Taylor instability. Basically it is the last condition which determines the final thickness of material which move inwards at a high velocity together with the fuel shell. In its compressed state the shell is not very thick, $\sim$10–20 μm in our calculations. Of course, if this shell is imploded by ablation it was initially much thicker and this is actually the case and is why the implosion is stable. During ablation the spikes or perturbations of the RT instability are eaten away while the shell becomes thinner. Since the instability decays exponentially inwards, the instability is prevented from growing and can even be damped out.

Let us now calculate $\eta_{\rm AP}$ in a simple approximation. We will consider the payload at the end of the main pulse, after ablation has finished. Then from conservation of momentum,

$$m_p v_p=m_{\rm Pb} V_{\rm Pb} \ , \tag{101}$$

where $v_p\sim 3\times 10^7$ cm/s, $m_{\rm Pb}$ is the mass of the lead tamper, and $v_{\rm Pb}$ is its outward velocity. At this point we assume that the payload moves inwards, the tamper outwards, and the lithium (lead) in between is stationary. Then

$$\eta_{AP}=\tfrac{1}{2}m_p v_0^2(m_c E_c+m_{Pb}E_{Pb}+\tfrac{1}{2}m_p v_0^2+\tfrac{1}{2}m_{Pb}v_{Pb}^2)^{-1}\ , \tag{102}$$

$$\eta_{AP}=\frac{m_p}{m_{Pb}}\left[2\left[\frac{m_c E_c+m_{Pb}E_{Pb}}{m_{Pb}v_0^2}\right]+\frac{m_p}{m_{Pb}}+\left[\frac{m_p}{m_{Pb}}\right]^2\right]^{-1}\ . \tag{103}$$

Let,

$$2\left[\frac{m_c E_c+m_{Pb}E_{Pb}}{m_{Pb}v_0^2}\right]=Bx+y^2\ , \tag{104}$$

$$B=\frac{2m_c}{m_p}\frac{E_c}{v_0^2}\ ,\quad y^2=\frac{2E_{Pb}}{v_0^2}\ ,\quad x=\frac{m_p}{m_{Pb}}\ . \tag{105}$$

Then

$$\eta_{AP}=x[y^2+(1+B)x+x^2]^{-1}\ , \tag{106}$$

where E_c is the energy/per gram needed to heat the cavity material to the working temperature T_0, m_c is the cavity mass, and E_{Pb} is the energy/per gram needed to heat the lead tamper.

At a maximum,

$$d\eta_{AP}/dx=0\ ,\quad x=m_p/m_{Pb}\ ,\quad m_p \text{ fixed at } m_p^0\ . \tag{107}$$

This leads to

$$x=x_0=y\ .$$

Therefore,

$$\eta_{AP}^{MAX}=\frac{y}{[2y^2+(1+B)y]}\ , \tag{108}$$

where, in this case,

$$m_{Pb}^0=ym_p^0 \text{ (fixed)} \tag{109}$$

for the efficiency to be a maximum.

Let us now assume that the ablation pressure is P_a.[14] Then

$$\frac{d}{dt}\left[m_p\frac{dR}{dt}\right]=-P_a 4\pi R^2\ , \tag{110}$$

where we use a simple model for the implosion which can be replaced by the homogeneous isentropic compression model of Kidder.[218–227] In this equation R is the shell radius, P_a is the ablation and thermal pressure generated by a radiation conduction wave, an ion-beam ablation wave, or ion-beam heating. Then

$$V_0^2=\frac{2}{3}\frac{P_a}{\rho_0\Delta R}\ , \tag{111}$$

where R_0 is the initial radius, ΔR_0 is the initial thickness, and ρ_0 the initial density,

$$P_a=\tfrac{3}{2}\rho_0 V_0^2(A)^{-1}\ , \tag{112}$$

where $A=R_0/\Delta R_0$ is the aspect ratio. This can be rewritten as

$$P_a V=\tfrac{1}{2}m_p v_0^2\ , \tag{113}$$

where m_p is the shell mass and $V=4\pi R_0^3$ is the initial volume. A or $R_0/\Delta R_0$ is fixed by the growth of the RT instability and the magnitude of the initial perturbations Δ_0.

$$R_0=\left[\frac{3m_p v_0^2}{8P_a}\right]^{1/3}\ , \tag{114}$$

$$m_p=m_F+m_p^{Pb/Li}\ , \tag{115}$$

$$m_p^{Pb/Li}=4\pi R_0^2\rho_0\Delta R_0\ , \tag{116}$$

where ΔR_0 is fixed by the maximum RT growth allowable. Thus m_F and R_0 fix the thickness of the fuel layer. Then m_p is fixed by Eq. (115) and m_{Pb} is fixed by the maximum-efficiency condition. The thickness of the lithium layer is fixed by the range shortening that occurs and the need for the lead to travel outwards. If it is too thin then the range comes back into the lead, and some lead travels inwards; if it is too thick then some material is heated which does not need to be heated. Thus the thickness of the layers can be determined. The ablation pressure is fixed by Eq. (113). The total energy needed is

$$\begin{aligned}E_{IB}&=P_a V+\tfrac{1}{2}m_{Pb}V_{Pb}^2+m_c E_c+m_{Pb}E_{Pb}\\&=\tfrac{1}{2}m_p V_0^2(1+y)+\tfrac{1}{2}m_p V_0^2 B+\frac{y^2V_0^2}{2}\frac{m_p}{y}\\&=\tfrac{1}{2}(m_p V_0^2)(1+y)+B+y\\&=\tfrac{1}{2}(m_p V_0^2)/(\eta_{AP}^{max})\ ,\end{aligned} \tag{117}$$

where m_p is determined by the mass of the fuel plus the RT instability thickness of the pusher shell.

The energy in the fuel is given by

$$E_F=\eta_{DF}E=\eta_{DF}E_{IB}\ . \tag{118}$$

η_{DF} has been determined above. From the mass of the fuel, the $(\rho R)_{fuel}$ and the mass of the hot spot one can determine the gain.[11,13,224,228] This depends on the distribution of E_F between hot-spot formation, compression, and heating of the rest of the fuel. The ablation pressure needed determines the power level of the beam. The ablation pressure itself is determined by R_0 or vice versa. Therefore the radius of the shell is determined by the power level available in the beam. Lower power levels mean larger pellets which, according to the stability analysis, remain stable.

In order to complete this zero-dimensional model[11,12] for the prediction of the gain we use a model developed by Long and Tahir in Refs. 11 and 12. This is an extension of a model developed by Kidder[224] and reviewed by Bodner.[226] In Kidder's model a constant density profile is assumed in the fuel. A constant-pressure model was developed by Meyer-ter-Vehn[228] but a general profile model was presented earlier by Long and Tahir[11,12] and as a two-density—two-temperature profile model in Ref. 12.

In this section we use the model developed in Refs. 11 and 12 because it includes this general fuel profile, the effect of tamping, a correct treatment of Fermi degeneracy, the energy of the ions, and symmetry considerations.

Only a simplified version is employed here. For full details see Refs. 11 and 12. The fuel configuration is shown in Fig. 2 in Ref. 12, where the hot spot, compressed region, and tamper are shown. A schematic diagram of the density and temperature profiles at ignition are given in Fig. 5,[12] see Fig. 23 for an actual example. The density and temperature of the hot spot are given by ρ_h and T_h, and the density and temperature of the compressed region are given by ρ_c and T_c. The radius of the hot spot must be greater than $R_\alpha(T_h)$ (Refs. 11, 12, 164, and 228), the range of α particles in DT at T_h, implying that $\rho_h R_h > 0.4$ g/cm^2 if 25% of α-particle energy is allowed to escape, or $\rho_h R_n > 0.8$ g/cm^2 if 12% can be allowed to escape in order to obtain ignition. In order to obtain ignition and nuclear and compressional heating must be greater than the losses due to α-particle escape and radiation (Bremsstrahlung) losses. The α-particle loss fractions for ρ_h and T_h can be estimated from formulas given in Refs. 140, and 229–231 as χ_{out},

$$\chi_{\text{out}}=\begin{cases}\frac{3}{4}\left(\frac{4}{3}-2\tau-\frac{16}{15}\tau^2\right), & 0\le\tau\le\frac{1}{2} \quad (119)\\ \frac{3}{4}\left[\frac{1}{3\tau}-\frac{1}{120\tau^3}\right], & \tau>\frac{1}{2}\ . \quad (120)\end{cases}$$

More complicated expressions have been worked out in Ref. 188 for the case where the reaction rate is of the form $a+br+cr^2$, where $\tau=(R_\alpha/R_F)^{-1}$, where R_α is the α-particle range and R_F is the fuel radius.

This was used in Refs. 142 and 164 as the basis for a fast method of computing α-particle transport. It is very useful and accurate for calculating the ignition temperature, see Figs. 7 and 8 in Ref. 164, where results for the HIBALL-I pellet are shown. Here the ignition temperature was found to be 8.5 KeV, with the inclusion of α-particle transport, compressional heating, nuclear reactions, and Bremsstrahlung radiation loss from the hot spot. The effect of neutron heating on the hot spot is small $\sim 3\%$ of α-particle heating.[164] Another condition on R_h is that is must be greater than εR_0 where ε is a symmetry factor[12,226] and R_0 is the initial radius of the fuel tamper shell. Therefore

$$R=\max(R_\alpha,\varepsilon R_0)\ . \quad (121)$$

In this model we use the "jellium" model of a plasma, in which the electrons are degenerate or nondegenerate as the case may be, and the ions move as a separate system and are treated as an ideal gas. Thus polarization effects are ignored[106] but could easily be included by the method due to Breuckner and Gell-Mann.[153–157] Then it can be shown that[11,12] for the electrons

$$E_T/Nk_BT=F_{3/2}(\eta')/F_{1/2}(\eta')\ , \quad (122)$$

$$1=\frac{3}{2}\left[\frac{k_BT}{E_F}\right]^{3/2}F_{1/2}(\eta')\ , \quad (123)$$

$$S/Nk_B=\tfrac{5}{3}[F_{3/2}(\eta')/F_{1/2}(\eta')]-\eta'\ , \quad (124)$$

where E_T is the total electron energy, $\eta'=\mu/k_BT$, where μ is the chemical potential and E_F is the Fermi energy, k_B is Boltzmann's constant. The value of η' is determined by solving Eq. (123), and $F_k(\eta')$, $k=\frac{1}{2},\frac{3}{2},\ldots$ are the well-known Fermi-Dirac integrals[232,233]

$$F_k(\eta')=\int\frac{x^k}{(e^{x-\eta'}+1)}dx\ , \quad (125)$$

S is the entropy, and the pressure is given by

$$P_E=\tfrac{2}{3}(E_T)/V\ , \quad (126)$$

where V is the volume, and P_E is the electron pressure. We use an enlarged hot spot to include the transition region between the hot spot and the compressed region, with a radius $R_h'=\frac{5}{4}R_h$. The mass of the enlarged hot spot m_h' is given by

$$m_h'=\tfrac{4}{3}\pi(R_h')^3B\rho_h$$
$$=2m_h\ , \quad (127)$$

where

$$m_h=\tfrac{4}{3}\pi R_h^3\rho_h\ . \quad (128)$$

The minimum ignition energy E_{IGN} (in J/g) is given by Ref. 12 as

$$\eta_{\text{DF}}E_{\text{IGN}}=m_h'e_h\ , \quad (129)$$

$$e_h=3k_BT_h/M_{\text{DT}}\ , \quad (130)$$

where η_{DF} is the driver fuel coupling efficiency calculated above, and M_{DT} is the mass of the DT ion. For a general mass m_F of the fuel, where $m_F>m_h'$, m_h' is heated to the ignition temperature T_h and the rest of the DT, m_F-m_h', is compressed to a density ρ_c at a temperature T_c. The energy per gram in the compressed region including both the partially degenerate electron and the ion contributions) is given by

$$e_c'=\left[\frac{k_BT_c}{M_{\text{DT}}}\right][\tfrac{3}{2}+F_{3/2}(\eta_c')/F_{1/2}(\eta_c')]\ . \quad (131)$$

The total energy in the compressed region is then

$$E_c=m_ce_c'\ , \quad (132)$$

$$m_c=m_F-m_h'\ . \quad (133)$$

Then

$$\eta_{\text{DF}}E_{\text{IB}}=E_{\text{fuel}}=(m_F-m_h')e_c'+m_h'e_h\ . \quad (134)$$

The $(\rho R)_{\text{fuel}}$ is given by

$$(\rho R)_{\text{fuel}}=\rho_hR_h'+\rho_cR_c\ . \quad (135)$$

The radius of the fuel $R_f=R_c+R_h'$ is given by

$$R_f=\left[\frac{\eta_{\text{DF}}E_{\text{IB}}+\frac{4}{3}\pi(R_h')^3e_c'-\frac{4}{3}\pi\rho_h(R_h')^3e_h}{\frac{4}{3}\pi\rho_ce_c'}\right]^{1/3}\ . \quad (136)$$

The fractional burn is given by[230]

$$\phi=(\rho R)_f/[\beta'+(\rho R)_f]\ , \quad (137)$$

where β' is $=6.3$ g/cm^2, $\beta'\propto\sqrt{T_B/\langle\sigma v\rangle}$, where T_B is the burn temperature and $\langle\sigma v\rangle$ is the DT cross section averaged over the Maxwell-Boltzmann distribution. The

gain is given by

$$Q=m_F\phi e_B/E_{\rm IB}\ , \tag{138}$$

where e_B is the fusion energy (J/g) for a 50:50 DT mixture equal to 3.4×10^{11} J/g. Results of this model for three efficiencies are given in Fig. 5 of Ref. 12.

This now completes the zero-dimensional analytic model developed here. Given the input energy and power it is now possible to predict the gain, the mass of the fuel, the inner radius of the target, the driver fuel coupling efficiency, and the masses and thickness of all the layers except the cavity layer. This seems to be fixed by considerations of range shortening and hydrodynamic stability. Clearly the lithium layer must be thick enough so that ions neither go into the fuel when the target is cold nor end in the tamper when the target is hot. The ion energy needed is fixed by the tamper and cavity-layer thicknesses. For a given cavity thickness there is clearly an optimum ion energy which maximizes $\eta_{\rm DF}$ due to the optimized thickness of the tamper layer. If ablation plays an important role the efficiency can be determined by use of the rocket-model formulas modified by the presence of the tamper. However, this must yield the same expression as Eq. (106) at the end of the implosion since this is derived on the basis of conservation of momentum.

In the rocket model if m_p^I is the initial mass of the payload and m_p^F is the final mass, moving with a velocity v_0, where u is the velocity of the ablating plasma in the target reference frame, then

$$m_p\frac{dv}{dt}=\frac{-udm_p}{dt}\rightarrow\frac{v_0}{u}=\ln\left[\frac{m_p^I}{m_p}\right]\ . \tag{139}$$

Then

$$\eta_{\rm AP}=\tfrac{1}{2}m_p^Fv_0^2/E_{\rm abs}=\left[\frac{v_0}{u}\right]^2\left[\exp\left[\frac{v_0}{u}\right]-1\right]\ . \tag{140}$$

However, this model is not easily applicable if there is tamping. This reduces u hence increasing the efficiency.

We have discussed briefly in Sec. IV A and Refs. 84 and 85 the compensation of range shortening by radiation transport. There we showed that the concept of Marshak waves[7,81–97] is useful. In this section we summarize some results of the motion of nonlinear radiation waves for various boundary-temperature–time variations.

For a boundary temperature of the form

$$T(0,t)=T_0t^P/t_0^P \tag{141}$$

we obtain the result[7,90]

$$X_w^2(t)=\frac{aT_0^3cl_Rt^{p(m+3)+1}}{(2.28C_vt_0^{p(m+3)}[1+p(m+4)]}\ , \tag{142}$$

where for $p=0$ we recover the constant boundary-temperature[7,84,85,95] case

$$X_w(t)=\left[\frac{aT_0^3cl_Rt}{2.28C_v}\right]^{1/2}\ . \tag{143}$$

The case of an exponential boundary-temperature variation with time has been derived in Ref. 7. In Eq. (142) $a=4\sigma/c$, where σ is the Stefan-Boltzmann constant, and c is the velocity of light, also

$$l_R=AT^m \tag{144}$$

and C_v is specific heat per unit volume. Numerical simulations and comparisons to these analytic solutions have been carried out in Refs. 7 and 83. These results show that the numerical methods used in this paper and Ref. 7 are correct.

We now consider a simple model of radiation-induced ablation, whereby we do not take into account the role of the tamper, or of hydrodynamic motion. Let us simply consider that a reduced power is heating the cavity material. This we denote by $P^R(t)$, where for constant deposition

$$P^R(t)=P_0(t)\left[1-\frac{R_L}{R_0}\right]\ , \tag{145}$$

where $R_0(E)$ is the range of the incident ions in lead, and R_L is the thickness of the lead. We assume that the power flow is used to heat up material and ablate it by the mechanism of a Marshak wave. Then

$$P^R(t)t=\rho_ax_w(t)C_g\ , \tag{146}$$

where ρ_a is the density of ablated material and C_g is the specific heat/per gram.

$$P^R(t)t=3\rho_ax_w(t)N_g[1+\overline{Z}(t)]\ , \tag{147}$$

where $\overline{Z}(t)$ is the degree of ionization and $N_g=1/m_i$ is the number of atoms per unit mass. We assume that

$$\overline{Z}(t)=\overline{A}T^\beta\ . \tag{148}$$

Let us also assume that

$$P^R(t)=P_0^Rt^\alpha\ ,\quad T=T_0t^p/t_0^p\ , \tag{149}$$

$$P_0^Rt^{\alpha+1}=\rho_a\overline{B}t^{(6p+1)/2}3N_g\overline{A}T^\beta\ ,$$

where $\beta=\frac{3}{2}$ and $\overline{B}$ is given from Eq. (142), $m=3$,

$$\overline{B}=\left[\frac{ac\,1_RT_0T_0^3}{2C_vt_0^{p(m+3)}[1+p(m+4)]}\right]^{1/2}\ , \tag{150}$$

$$P_0^Rt^{\alpha+1}=\rho_a\overline{A}\overline{B}t^{(6p+1)/2}3N_g\frac{T_0^{3/2}}{t_0^{3p/2}}t^{3p/2}\ , \tag{151}$$

$$(\alpha+1)=\frac{6p+4+1+3p}{2}\ , \tag{152}$$

$$p=[2(\alpha+1)-1]/9\ , \tag{153}$$

$\alpha=0$, $p=\frac{1}{9}$; $\alpha=1$, $p=\frac{1}{3}$; $\alpha=2$, $p=\frac{5}{9}$; $\alpha=3$, $p=\frac{7}{9}$; $\alpha=4$, $p=1$.

If the Marshak wave is causing ablation, then the ablation pressure is given by

$$P_{\rm abl}=\frac{\rho_a^2}{\rho_s}\dot{x}_w(t)^2\ , \tag{154}$$

where ρ_s is the density of the ablated material, for $\alpha=1$, $p=\frac{1}{3}$, and $P_{\rm abl}$ increases linearly with time.

$$P_{\rm abl}=\frac{\rho_a^2}{\rho_s}\frac{acl_R(T_0)T_0^3 t^{p(m+3)-1}}{2.28C_v t_0^{p(m+3)}\phi(p)}\frac{[p(m+3)+1]^2}{4}, \quad (155)$$

$$\phi(p)=[1+p(m+4)]$$

for $\alpha=2$, $p=\frac{5}{9}$, and

$$P_{\rm abl}\propto t^{21/9}=t^{7/3}. \quad (156)$$

Thus the ablation pressure rises linearly with time when the power is rising linearly in time. It rises as t^2 when the power rises as t^2. For a full treatment of this problem one should include the hydrodynamic flow but this is more complicated when one has a tamper.

B. Discussion and conclusions

It has been clearly shown in this paper that the detailed physics of the energy loss of ions in hot dense plasmas plays an important role in ion-beam-driven fusion pellet implosions. The physical behavior of the ions can lead to problems in obtaining ignition but it is also advantageous in avoiding for instance, radiation preheat or preheat from knock-on ions. In Secs. II A and II B we have discussed some aspects and problems of the theory of the calculation of the energy loss of ions in dense plasmas. We have emphasized that the distinction between bound- and free-electron states is an oversimplification, because in fact the states change gradually from one to the other as the energy increases. Also problems connected with degeneracy, nonideality, and more detailed calculations of electronic states in the disordered potentials existing in the plasma, as well as the atomic electron states within the plasma background, must be solved. Calculations have been presented using a definite physical model and were compared briefly to other methods. The energy deposition of charged particles during ignition and burn has been briefly discussed. We have presented a method of coupling microscopic energy-deposition data into any hydrodynamic code and analyzed its efficacy by giving examples. The physics in the MEDUSA code, especially the extensions, have been described. Using this renovated and extended version of the coupled code we have carried out detailed numerical simulations of various reactor-size target designs for heavy ion beams. It was shown possible to compensate for range shortening by ion voltage ramping and/or radiation transport. It was discovered that one or the other mechanism dominates depending on which can move the ablation front fastest and that these two effects do no add linearly. It seems one can only heat the plasma, one way or the other (reminding one of the saying that you do and you do not step into the same river twice). Initially it appears that range shortening is deleterious because one loses ignition, due to the increase in the payload mass. However, this effect can be used to advantage by compensating for this range shortening by ion-beam-driven ablation or radiation-driven ablation. Both produce very smooth, gradual implosions with gentler or gentle density gradients. This occurs to such an extent that it was found that using various new analyses of the Rayleigh-Taylor instability including ablation, thermal conduction, compressibility, and ablation-induced density profiles that these implosions appear to be stable, in the sense that growth rates are tolerable, and that later on the instability appears to be damped out. Actual density profiles appear to be even more favorable, if they were to be combined with the self-consistent linear analysis used. However, one needs detailed two-dimensional simulations or theory to confirm these results. In fact, a one-dimensional theory including all these phenomena would be very useful as it would, it is hoped, confirm these numerical results. One possible such theory was discussed rather briefly due to lack of space, but this tends to confirm that slow ablatively driven implosions of thin shells are stable, i.e., do not lead to shell breakup . The targets used all gave high gains, and the various target designs were compared both from a physics point of view and from the reactor point of view, i.e., cost and ease of fabrication. In general, the HIBALL-I design was found to be more stable than the HIBALL-II design. An interesting HIBALL-II design is, however, one with a very thick lead-gold or even, say, aluminum layer into which ions are gradually driven. At first material is compressed and then the ions penetrate into this compressed layer giving increased energy deposition per gram.

This may increase the hydrodynamic efficiency although one would need to prove this by a very careful analysis. However, it is always a question as to whether the extra cost introduced by extra layers in the target is offset by the increased gain. In general, all these targets have a high gain, and with reasonable input energies. In view of the good stability situation the power can be reduced by having larger targets (with a larger inner radius) and thinner layers. It is an interesting question whether or not various targets can have lower input energies for the same gain. However, the stability situation would always have to be carefully monitored. The materials used in these pellets are compatible with the reactor system and lead to a manageable radioactivity problem. We have also discussed how pellet heating in the reactor chamber effects pellet performance via the generation of a DT vapor pressure in the void.

A detailed zero-dimensional analytic model has been discussed which has proved very useful in designing these pellets and in interpreting the results. It is also very useful for providing ideas on how to improve pellet performance. For a given pellet fuel mass, it allows one to design the target by fixing layer thicknesses and to fix the energy input and the power levels for a given gain and a given inner radius. The mass of the fuel is also related to the gain and the input energy. Thus one can considerably reduce the number of variable parameters and make pellet tuning considerably easier. The achievement of ignition through shock timing has also been analyzed. Improved methods of obtaining ignition allow one to reduce power and energy levels substantially, by reducing the necessary pusher velocity.

Finally, one can say that any deleterious effects of range shortening on ion-beam pellet performance have been banished and in fact range shortening has proved to be advantageous because of the reduction of preheat, the improvement of stability, and the simplification of the pellet structure. The pellets designed here, in particular,

the proposed HIBALL design for the HIBALL-I target design have been proved to be admirably suited for use in a future reactor system as proposed in Refs. 7—11 and 234. Of course, one cannot rule out that additional physics effects could reduce pellet performance, such as frequency-dependent radiation transport or plasma effects on the effective charge. Much larger range shortening than the already large effects seen here could cause problems, especially if one wants or has to compensate by radiation transport. On the other hand, compensation by voltage ramping is always possible from a theoretical point of view. But it may be difficult to do this in practice. However, dual energy beams should be able to be produced and these would probably be sufficient. Here one would have one energy for the prepulse and the beginning of the main pulse and another larger ion energy for the remainder of the main pulse. The ion energies would be fixed so that no ions would go into the fuel, although this has also been proposed.

ACKNOWLEDGMENTS

One of the authors (K.A.L.) would like to thank Professor J. Ligou and Professor Schneeberger for discussions on the contents of this paper and for the stay at Lausanne, where this paper was written.

[1]K. A. Long, N. Moritz, and N. A. Tahir, Kernforschungszentrum Karlsruhe Report No. KfK-3608, 1983 (unpublished).
[2]J. P. Christiansen, D. Ashby, and K. V. Roberts, Comput. Phys. Commun. **7**, 721 (1974).
[3]K. A. Long, N. A. Tahir, Kernforschungszentrum Report No. KfK-3232, 1981 (unpublished).
[4]R. G. Evans (private communication).
[5]N. A. Tahir and K. A. Long, Kernforschungzentrum Karlsruhe Report No. KfK-3454, 1983 (unpublished).
[6]K. A. Long and N. A. Tahir, in Proceedings of the Rutherford Conference on Atomic Physics for ion beam fusion, Oxford, 1984 (unpublished).
[7]K. A. Long and N. A. Tahir, Laser Part. Beams **4**, 287 (1986).
[8]B. Badger *et al.*, University of Wisconsin—Madison Report No. UWFDM-750, 1981 (unpublished); Kernsforschungszentrum Report No. KfK-3202, 1981 (unpublished).
[9]R. Bangeter, in Proceedings of the Conference on Heavy Ion Accelerators and their Applications to Inertial Fusion, Tokyo, 1985 (unpublished).
[10]C. Deutsch, Ann. Phys. (Paris) **11**, 1 (1986).
[11]N. A. Tahir and K. A. Long, Atomkernenergie **40**, 157 (1982).
[12]K. A. Long and N. A. Tahir, Phys. Lett. **91A**, 451 (1982).
[13]N. A. Tahir and K. A. Long, Phys. Lett. **90A**, 242 (1982).
[14]N. A. Tahir and K. A. Long, Nucl. Fusion **23**, 887 (1983).
[15]R. Bangeter and D. Meeker, University of California Radiation Laboratory Report No. UCRL-78474, 1976 (unpublished).
[16]M. J. Clauser, Phys. Rev. Lett. **35**, 848 (1975).
[17]M. A. Sweeney and A. V. Farnsworth, Nucl. Fusion **21**, 41 (1981).
[18]D. Havazelet, M. Sapir, and T. J. Bar-noy, J. Phys. D **16**, 315 (1983).
[19]M. Tamba, N. Nagata, S. Kawata, and K. Niu, Laser Part. Beams **2**, 121 (1983).
[20]F. C. Young, D. Mosher, S. J. Stepanakis, S. A. Goldstein, and T. A. Mehlhorn, Phys. Rev. Lett. **49**, 549 (1982).
[21]D. Mosher, G. Cooperstein, S. J. Stepanakis, S. Goldstein, D. T. Colombant, and R. Lee, Naval Research Laboratory Report No. 3658, 1977 (unpublished).
[22]K. A. Long, Yu. S. Sayasov, and N. A. Tahir, in Proceedings of the Rutherford Conference on Atomic Physics for Ion Beam Fusion, Oxford, 1985 (unpublished).
[23]K. A. Long and N. A. Tahir, Phys. Fluids **29**, 275 (1986).
[24]C. R. Devore, J. H. Gardner, J. P. Boris, and D. Mosher, Laser Part. Beams **2**, 227 (1984).
[25]G. R. Magelssen, Nucl. Fusion **24**, 1527 (1984).
[26]G. R. Magelssen and W. Gula, Phys. Fluids **25**, 898 (1982).
[27]Proceedings of the Conference on Accelerator Aspects of Heavy Ion Fusion, Darmstadt, Federal Republic of Germany, 1982 (unpublished).
[28]Proceedings of the Conference on Heavy Ion Accelerators and their Applications to Inertial Fusion, Tokyo 1984 (unpublished).
[29]Gesellschaft für Schwerionenforschung Darmstadt Annual Report No. GSI-81-3, 1981 (unpublished).
[30]Gesellschaft für Schwerionenforschung Darmstadt Annual Report No. GSI-82-6, 1982 (unpublished).
[31]Gesellschaft für Schwerionenforschung Darmstadt Annual Report No. GSI-83-2, 1983 (unpublished).
[32]Gesellschaft für Schwerionenforschung Darmstadt Annual Report No. GSI-84-5, 1984 (unpublished).
[33]Gesellschaft für Schwerionenforschung Darmstadt Annual Report No. GSI-85-21, 1985 (unpublished).
[34]N. A. Tahir, K. A. Long, and R. Fröhlich, in Ref. 27, p. 598.
[35]G. Sawyer *et al.*, Los Alamos Laboratory Report No. LA-8207-MS, 1980 (unpublished).
[36]R. O. Bangeter, J. Mark, and A. Thiessen, Phys. Lett. **88A**, 225 (1982).
[37]S. Nakai, K. Imasaki, S. Miyamoto, S. Higaki, T. Ozaki, A. Yoshinouchi, H. Fujita, K. Mika, K. Nishihara, T. Yabe, S. Ido, Y. Ohgaki, and C. Yamanaka, Laser Part. Beams **1**, 29 (1983).
[38]G. Yonas and A. Toepfer, *Gaseous Electronics* (Academic, New York, 1978), Vol. 1, chap. 6.
[39]S. Humphries, Nucl. Fusion **20**, 1549 (1980).
[40]N. A. Tahir and K. A. Long, in Ref. 30, p. 53.
[41]N. A. Tahir and K. A. Long, in Ref. 30, p. 59.
[42]N. A. Tahir and K. A. Long, in Ref. 31, p. 38.
[43]N. A. Tahir and K. A. Long, in Ref. 32, p. 74.
[44]S. Humphries, C. Eichenberger, and R. Sudan, J. Appl. Phys. **48**, 2738 (1977).
[45]R. Sudan and R. Lovelace, Phys. Rev. Lett. **31**, 1174 (1973).
[46]R. Sudan and A. Mankofsky, Nucl. Fusion **24**, 827 (1984).
[47]F. Winterberg, Phys. Rev. **174**, 212 (1968).
[48]R. E. Kidder, Nucl. Fusion **14**, 953 (1974).
[49]H. Hora, *Physics of Laser Driven Plasmas* (Wiley, New York, 1981).
[50]J. H. Nuckolls, in *Laser Interaction and Related Plasma Phenomena,* edited by H. J. Schwarz and H. Hora (Plenum, New York, 1974), Vol. 3, p. 399.

[51]J. Nuckolls, L. Wood, A. Thiessen, and G. Zimmermann, Nature (London) **239**, 139 (1972).
[52]J. Clarke, H. Fischer, and R. Mason, Phys. Rev. Lett. **30**, 89 (1973).
[53]K. Breuckner, Electric Power Research Institute Report No. EPRI-AP-1371, 1980 (unpublished).
[54]K. Breuckner and S. Jorna, Rev. Mod. Phys. **46**, 325 (1974).
[55]C. Yamanaka, in Ref. 28, p. 56.
[56]Yu. V. Afanasiev, N. G. Basov, V. A. Danilychev, A. G. Melchanov, and P. N. Lebedev, in Ref. 28, p. 58.
[57]J. W. Shearer, Nucl. Fusion **15**, 952 (1975).
[58]E. Nardi, E. Peleg, and Z. Zinamon, Phys. Fluids **21**, 574 (1978).
[59]E. Nardi and Z. Zinamon, Phys. Fluids **24**, 1527 (1981); Phys. Rev. Lett. **49**, 1251 (1982).
[60]R. M. More, University of California Radiation Laboratory Report No. UCRL-84115, 1980 (unpublished); D. Bailey, Y. T. Lee, and R. M. More, J. Phys. (Paris) Colloq. **44**, C8-149 (1983).
[61]T. Beynon, Philos. Trans. R. Soc. London, Ser. A **300**, 613 (1982).
[62]T. A. Mehlhorn, J. Appl. Phys. **52**, 6522 (1981).
[63]T. A. Mehlhorn, J. M. Peek, E. J. McGuire, J. N. Olsen, and F. Young, J. Phys. (Paris) Colloq. **44**, C8-39 (1983).
[64]C. Deutsch, G. Maynard, and H. Minoo, in Ref. 27, p. 543.
[65]K. A. Long and N. A. Tahir, in Ref. 29, p. 29.
[66]K. A. Long and N. A. Tahir, in Ref. 30, p. 54.
[67]K. A. Long and N. A. Tahir, in Ref. 31, p. 57.
[68]J. Meyer-ter-Vehn and N. Metzler, in Ref. 29, p. 33.
[69]R. Swegele, Comments Plasma Phys. Controlled Fusion **7**, 141 (1982).
[70]D. Miller, *An Introduction to the Physics of Intense Charged Particle Beams* (Plenum, London, 1982).
[71]D. Mosher, D. G. Colombant, S. Goldstein, and P. F. Ottinger, in *Proceedings of the Conference on High Power Beams,* edited by H. J. Doucet and J. M. Buzzi (CNRS, Palaiseau, France, 1981), Vol. 1, p. 19.
[72]J. R. Freeman, L. Baker, and D. L. Cook, in Ref. 71, p. 121.
[73]P. E. Ottinger, S. A. Goldstein, and R. A. Meger, NRL Memorandum, Report No. 5205, 1983 (unpublished).
[74]R. A. Meger, R. J. Commisso, G. Cooperstein, and S. A. Goldstein, NRL Memorandum Report No. 5037, 1983 (unpublished).
[75]G. A. Moses and R. Peterson (private communication).
[76]N. A. Tahir and K. A. Long, in Ref. 31, p. 58.
[77]N. A. Tahir and K. A. Long, in Ref. 31, p. 59.
[78]N. Metzler and J. Meyer-ter-Vehn, Laser Part. Beams **2**, 27 (1984).
[79]G. Velarde, C. Ahnert, J. M. Aragones, M. Gomez-Alomso, G. Leira, R. Luqui, J. M. Martinze-Val, and M. Pelardo, Atomkernenergie **35**, 40 (1980).
[80]K. A. Long and N. A. Tahir, in Ref. 32, p. 71.
[81]K. A. Long and N. A. Tahir, in Ref. 33.
[82]K. A. Long and N. A. Tahir, in Ref. 33.
[83]N. A. Tahir and K. A. Long, Laser and Particle Beams **2**, 371 (1984).
[84]K. A. Long and N. A. Tahir, Phys. Fluids **29**, 4204 (1986).
[85]N. A. Tahir and K. A. Long, Phys. Fluids **29**, 1282 (1986).
[86]N. A. Tahir and K. A. Long, in Ref. 33.
[87]N. A. Tahir and K. A. Long, in Ref. 33.
[88]K. A. Long, N. A. Tahir, and G. C. Pomraning, in Ref. 31, p. 39.
[89]K. A. Long and N. A. Tahir, in Ref. 32, p. 51.
[90]K. A. Long and N. A. Tahir, Z. Phys. A, **325**, 99 (1986).
[91]N. A. Tahir and K. A. Long, in Ref. 32, p. 75.
[92]G. C. Pomraning, *Radiation Hydrodynamics* (Pergamon, London, 1973).
[93]G. C. Pomraning, J. Appl. Phys. **38**, 3845 (1967).
[94]R. Marshak, Phys. Fluids **1**, 24 (1958).
[95]A. Petschek, R. Williamson, and J. Wooten, Los Alamos Natl. Lab. Report No. LAMS-2421, 1960 (unpublished).
[96]Ya. B. Zel'dovich and Yu. P. Raizer, *Physics of Shock Waves and High Temperature Phenomena* (Academic, London, 1966), Vols. 1 and 2.
[97]R. Pakula and R. Sigel, Phys. Fluids **28**, 232 (1985).
[98]K. Breuckner, L. Senbetu, and N. Metzler, Phys. Rev. B **25**, 4377 (1982).
[99]K. A. Long, Doctoral thesis, London University, Imperial College, 1971.
[100]Yu. S. Sayasov, J. Phys. (Paris) Colloq. **44**, C8-1 (1983).
[101]L. P. Kadanoff and G. Baym, *Quantum Statistical Mechanics* (Benjamin, New York, 1962).
[102]N. H. March, in *The Theory of the Inhomogeneous Electron Gas,* edited by N. H. March and S. Lundquist (Plenum, New York, 1983), p. 1.
[103]N. H. March, Adv. Phys. **6**, 1 (1957).
[104]D. Kirznitz, Sov. Phys.—JETP **8**, 1081 (1959).
[105]W. Geiger, H. Hornberg, and K. H. Schramm, *Zustand der Materie unter sehr hohem Druck und Temperatur,* Vol. 46 of *Springer Tracts in Modern Physics,* edited by G. Höhler (Springer-Verlag, Berlin, 1968).
[106]S. Doniach and E. H. Sondheimer, *Green's Functions for Solid State Physicists* (Benjamin, New York, 1972); S. Ichimaru, *Basic Principles of Plasma Physics* (Benjamin, New York, 1973).
[107]A. A. Abriksov, L. P. Gor'kov, and L. E. Dzyloskinskii, *Methods of Quantum Field Theory in Statistical Physics* (Prentice-Hall, Englewood Cliffs, 1963).
[108]G. Maynard and C. Deutsch, Phys. Rev. A **26**, 665 (1982).
[109]J. Lindhard, K. Dan. Vidensk. Selsk. Mat. Fys. Medd. **28**, No. 8 (1954).
[110]J. Lindhard, M. Scharff, and H. E. Schiøtt, K. Dan. Vidensk. Selsk. Mat. Fys. Medd. **33**, No. 14 (1963).
[111]J. Lindhard and A. Winther, K. Dan. Vidensk. Selsk. Mat. Fys. Medd. **34**, No. 4 (1964).
[112]S. Chandrasekhar, *Principles of Stellar Dynamics* (Dover, New York, 1960), p. 251.
[113]S. Chandrasekhar, Rev. Mod. Phys. **15**, 1 (1943).
[114]L. Spitzer, *Physics of Fully Ionized Gases,* 2nd ed. (Wiley, New York, 1962).
[115]N. A. Krall and A. W. Trivelpiece, *Principles of Plasma Physics* (McGraw-Hill, New York, 1973).
[116]H. A. Bethe, Ann. Phys. (Leipzig) **5**, 325 (1936).
[117]H. A. Bethe, *Quantenmechanik der Ein- und Zweiphasen-Elektronenprobleme,* Vol. 24 of *Handbuch der Physik* (Springer-Verlag, Berlin, 1933), p. 273.
[118]N. Bohr, K. Dan. Vidensk. Selsk. Mat. Fys. Medd. **18**, No. 8 (1948).
[119]N. Bohr, Philos. Mag. **30**, 581 (1915).
[120]S. P. Ahlen, Rev. Mod. Phys. **52**, 121 (1980).
[121]J. J. Thomson, *Conduction of Electricity Through Gases* (Cambridge University, Cambridge, England, 1903).
[122]N. F. Mott, Ann. Phys. (Leipzig) **16**, 285 (1933).
[123]F. Bloch, Ann. Phys. (Leipzig) **16**, 285 (1933).
[124]F. Bloch, Z. Phys. **81**, 363 (1933).
[125]J. A. Ball, J. A. Wheeler, and E. L. Fireman, Rev. Mod. Phys. **45**, 333 (1973).
[126]R. Bangeter, Argonne National Laboratory Report No.

ANL-79-41, 1979 (unpublished).
[127]D. Mosher, Lawrence-Berkeley Laboratory Report No. LBL-5543, 1976 (unpublished).
[128]C. Deutsch, G. Maynard, and H. Minoo, J. Phys. (Paris) Colloq. **44**, C8-67 (1983).
[129]K. A. Long, Atomic Energy Research Establishment Harwell Report No. AERE/EMR-PR-2277(2), 1974 (unpublished).
[130]C. Gouedard and C. Deutsch, J. Math. Phys. **19**, 32 (1978).
[131]Yu. S. Sayasov, Z. Phys. A **313**, 9 (1983).
[132]Yu. S. Sayasov and K. A. Long, Proceedings of the Rutherford Conference on Atomic Physics for Ion Beam Fusion, Oxford, 1986 (unpublished).
[133]M. Basko, Institute of Theoretical and Experimental Physics Report No. ITEP-113, 1983 (unpublished).
[134]N. F. Mott and H. Jones, *The Theory of the Properties of Metals and Alloys* (Oxford University Press, London, 1936).
[135]C. Kittel, *Solid State Physics* (Wiley, New York, 1968).
[136]N. F. Mott, *Metal Insulator Transitions* (Taylor and Francis, London, 1974).
[137]P. W. Anderson, Phys. Rev. **109**, 1492 (1958).
[138]P. W. Anderson, *Basic Notions of Condensed Matter Physics* (Benjamin, New York, 1984).
[139]K. A. Long and N. A. Tahir, in Ref. 30, p. 56.
[140]K. A. Long and N. A. Tahir, in Ref. 30, p. 55.
[141]K. A. Long and N. A. Tahir, in Ref. 31, p. 57.
[142]K. A. Long and N. A. Tahir, in Ref. 32, p. 63.
[143]P. Haldy, Doctoral thesis, No. 379, Ecole Polytechnique Féderale de Lausanne, 1980.
[144]T. M. Tran, Doctoral thesis, Ecole Polytechnique, Féderale de Lausanne, 1983.
[145]P. Haldy and J. Ligou, Nucl. Fusion **17**, 1225 (1977).
[146]T. M. Tran and J. Ligou, Nucl. Sci. Eng. **79**, 269 (1981).
[147]M. Rosenbluth, W. M. Macdonald, and D. L. Judd, Phys. Rev. **107**, 1 (1957).
[148]P. S. Ray and H. Hora, Z. Naturforsch. Teil A **32**, 538 (1977).
[149]A. N. Cox, in *Stellar Structures,* edited by L. Aller and B. McLaughlin (University of Chicago Press, Chicago, 1965).
[150]S. Rosznai, J. Quant. Spectros. Radiat. Transfer **15**, 695 (1975).
[151]W. Heubner, A. Mertz, N. Magee, and M. Argo, Los Alamos Scientific Laboratory Report No. LA-6760-M, 1977 (unpublished).
[152]R. Latter, Phys. Rev. **99**, 1854 (1955).
[153]D. Bohm and D. Pines, Phys. Rev. **92**, 609 (1953)
[154]D. Pines, *Elementary Excitations* (Benjamin, New York, 1965).
[155]D. Pines and P. Nozières, *Theory of Quantum Fluids* (Benjamin, New York, 1966), Vol. 1.
[156]P. Noziéres, *Theory of the Interacting Fermi Gas* (Benjamin, New York, 1964).
[157]M. Gell-Mann and K. Breuckner, Phys. Rev. **106**, 364 (1957).
[158]R. H. Ritchie, Phys. Rev. **106**, 874 (1957).
[159]R. H. Ritchie, Phys. Rev. **114**, 664 (1959).
[160]J. Hubbard, Proc. R. Soc. London Ser. A **68**, 978 (1955).
[161]E. Fermi, Phys. Rev. **57**, 485 (1940).
[162]G. S. Fraley, E. J. Linnebur, R. J. Mason, and R. L. Morse, Phys. Fluids **17**, 414 (1974).
[163]J. Duderstadt and G. A. Moses, *Inertial Confinement Fusion* (Wiley, New York, 1982).
[164]K. A. Long and N. A. Tahir, Nucl. Fusion **26**, 555 (1986).
[165]S. Skupsky, Phys. Rev. A **16**, 727 (1977).
[166]N. R. Arista and W. Brandt, Phys. Rev. A **23**, 1898 (1981).
[167]J. J. Devaney and M. L. Stein, Nucl. Sci. Eng. **46**, 523 (1971).
[168]D. G. Yakovlev and S. S. Kotel'nikov, Sov. Phys—JETP **57**, 781 (1983).
[169]S. V. Bozhokin and E. A. Choban, Sov. J. Plasma Phys. **9**, 242 (1983).
[170]M. D. Brown, and C. D. Moak, Phys. Rev. B **6**, 90 (1972).
[171]J. von Neumann and R. D. Richtmeyer, J. Appl. Phys. **21**, 232 (1950).
[172]A. Bell, Rutherford Laboratory Report No. RL-50-091, 1980 (unpublished).
[173]B. Bennett, J. Johnson, G. Kerley, and G. Rood, Los Alamos Scientific Laboratory Report No. LA-7130, 1978 (unpublished).
[174]K. A. Long and N. A. Tahir, in Ref. 30. p. 55.
[175]J. P. Christiansen and K. V. Roberts, Comput. Phys. Commun. **7**, 245 (1974).
[176]N. A. Tahir and E. W. Laing, Phys. Lett. **77A**, 430 (1980).
[177]N. A. Tahir, K. A. Long, and E. W. Laing, J. Appl. Phys. **60**, 898 (1986).
[178]G. A. Moses, University of Wisconsin—Madison Report No. UWFDM-198, 1977 (unpublished).
[179]G. A. Moses, Nucl. Sci. Eng. **64**, 49 (1977).
[180]B. Goel and H. Henderson, in Ref. 27, p. 626.
[181]G. A. Moses and R. A. Peterson (private communication).
[182]G. M. Rosenblatt, in *Treatise on Solid State Chemistry,* edited by N. B. Hannay (Plenum, New York, 1976), Vol. 6A.
[183]O. Knacke and I. N. Stranski, Prog. Met. Phys. **6**, 181 (1956).
[184]J. P. Hirth and G. M. Pound, *Condensation and Evaporation,* Vol. II of *Progress in Materials Science* (Pergamon, New York, 1963).
[185]C. Briggs, R. Hickmann, R. Tsugawa, and P. Souers, in Proceedings on Radiation Effects and Tritium Technology for Fusion Reactors, Gatlinburg, 1979 (unpublished).
[186]H. M. Roder, G. E. Childs, R. D. McCarthy, and P. E. Angerhofer, Natl. Bur. Stand. (U.S.) Technical Note 641, 1973 (unpublished).
[187]C. Cercignani, *Theory and Application of the Boltzmann Equation* (Scottish Academic Press, Edinburgh and London, 1975).
[188]C. Cercignani, *Mathematical Methods in Kinetic Theory* (MacMillan, London, 1969).
[189]M. N. Kogan, *Rarified Gas Dynamics* (Plenum, New York, 1969).
[190]B. Brunelli, Nuovo Cimento **B55**, 264 (1980).
[191]S. Atzeni and A. Caruso, Nuovo Cimento **B64**, 383 (1981).
[192]H. Anderson and J. Ziegler, *Hydrogen Stopping Power and Ranges in All Elements* (Pergamon, New York, 1977).
[193]F. Winterberg, *The Physical Principles of Thermonuclear Explosive Devices* (Fusion Energy Foundation, New York, 1981).
[194]R. Bangeter (private communication); Proceedings of the Rutherford Conference on Atomic Physics for Ion Beam Fusion, Oxford, 1985 (unpublished).
[195]A. Pritzke, SIN (Switzerland) Report No. TM-37-18, 1982 (unpublished).
[196]E. Nardi and Z. Zinamon, Phys. Rev. A **20**, 1197 (1979).
[197]J. Lindl and W. Mead, Phys. Rev. Lett. **34**, 1273 (1975).
[198]K. O. Mikaelian, Phys. Rev. A **26**, 2140 (1982).
[199]R. McCrory, R. Morse, and K. A. Taggart, Nucl. Sci. Eng. **64**, 163 (1977).
[200]K. O. Mikaelian, Phys. Rev. A **28**, 1637 (1983).
[201]K. O. Mikaelian, Phys. Rev. A **29**, 290 (1984).
[202]K. O. Mikaelian, and L. Lindl, Phys. Rev. **48**, 1365 (1982).
[203]Lord Rayleigh, Proc. R. Soc. London, Ser. A **14**, 170 (1983).
[204]G. Taylor, Proc. R. Soc. London, Ser. A **201**, 192 (1950).
[205]S. Bodner, Phys. Rev. Lett. **32**, 761 (1974).

[206]H. Takabe, L. Montierth, and R. Morse, Phys. Fluids **26**, 2299 (1983).
[207]H. Takabe, Institute for Laser Engineering Osaka Report No. ILE-QPR-83-6, 28 1983 (unpublished); Phys. Fluids **28**, 3676 (1985).
[208]S. Chandrasekhar, *Hydrodynamic and Hydromagnetic Stability* (Oxford University Press, London, 1961).
[209]H. Kull, Phys. Rev. Lett. **51**, 1434 (1983).
[210]H. Jacobs, Kernforschungszentrum Karlsruhe, Report No. KfK-3756, 1984 (unpublished).
[211]G. Buchwald, D. Barthel, J. Cieza, and J. A. Mahruhn, in Ref. 33, p. 56.
[212]H. Hora and A. K. Ghatak, Phys. Rev. A **31**, 3473 (1985).
[213]H. Hora, Laser Part. Beams **3**, 59 (1983).
[214]R. G. Evans, Laser Part. Beams **1**, 231 (1983).
[215]B. Ahlborn, J. Phys. Soc. Jpn. **50**, 3767 (1981).
[216]H. Kull and S. Anisimov, Phys. Fluids **29**, 2067 (1986).
[217]M. H. Emery, J. H. Gardner, and S. E. Bodner, Phys. Rev. Lett. **57**, 703 (1986).
[218]C. Max, C. McKee, and W. Mead, Phys. Fluids **23**, 1620 (1980).
[219]B. Ahlhorn, M. Key, and A. Bell, Phys. Fluids **25**, 541 (1982).
[220]M. H. Key, *Proceedings of the Twentieth Scottish Summer School* (SUSP, Edinburgh, 1979), p. 219.
[221]R. E. Kidder, Nucl. Fusion **14**, 53 (1974).
[222]R. E. Kidder, Nucl. Fusion **14**, 794 (1974).
[223]R. E. Kidder, Nucl. Fusion **16**, 3 (1976).
[224]R. E. Kidder, Nucl. Fusion **16**, 405 (1976).
[225]R. E. Kidder, Nucl. Fusion **19**, 223 (1979).
[226]S. Bodner, J. Fusion Energy **1**, 221 (1981).
[227]R. Mason and R. Morse, Los Alamos Scientific Laboratory Report No. LA-5789-MS, 1974 (unpublished).
[228]J. Meyer-ter-Vehn, Nucl. Fusion **22**, 561 (1982).
[229]O. N. Krokhin and V. B. Rozanov, Sov. J. Quantum Electron. **2**, 393 (1973).
[230]M. J. Antal and C. E. Lee, J. Comput. Phys. **20**, 298 (1976).
[231]R. S. Cooper and F. Evans, Phys. Fluids **18**, 332 (1975).
[232]J. MacDougal and E. C. Stoner, Philos. Trans. R. Soc. London **67**, 237 (1983).
[233]E. C. Stoner, Philos. Mag. **28**, 257 (1939).
[234]B. Badger *et al.*, Kernforschungszentrum Report No. KfK-3840, 1985 (unpublished).